

## RESEARCH ARTICLE

10.1029/2017JB015163

## Key Points:

- The 23 February 2013 Etna eruption features were reconstructed integrating tephra, satellite, and aerosol optical depth measurements
- Synergetic use of field and satellite data to assess the total grain-size distribution from coarse lapilli to very fine ash
- Simultaneous numerical simulations of the tephra loading and airborne ash dispersal

## Supporting Information:

- Supporting Information S1
- Figure S1
- Figure S2
- Figure S3

## Correspondence to:

M. Poret,  
matthieu.poret@gmail.com

## Citation:



Poret, M., Costa, A., Andronico, D., Scollo, S., Gouhier, M., & Cristaldi, A. (2018). Modeling eruption source parameters by integrating field, ground-based, and satellite-based measurements: The case of the 23 February 2013 Etna paroxysm. *Journal of Geophysical Research: Solid Earth*, 123. <https://doi.org/10.1029/2017JB015163>

Received 27 OCT 2017

Accepted 2 JUN 2018

Accepted article online 9 JUN 2018

## Modeling Eruption Source Parameters by Integrating Field, Ground-Based, and Satellite-Based Measurements: The Case of the 23 February 2013 Etna Paroxysm

M. Poret<sup>1,2</sup> , A. Costa<sup>1</sup> , D. Andronico<sup>3</sup>, S. Scollo<sup>3</sup>, M. Gouhier<sup>4</sup>, and A. Cristaldi<sup>3</sup>

<sup>1</sup>Istituto Nazionale di Geofisica e Vulcanologia, Bologna, Italy, <sup>2</sup>Geophysics Department, University of Bologna, Bologna, Italy, <sup>3</sup>Istituto Nazionale di Geofisica e Vulcanologia, Osservatorio Etneo, Catania, Italy, <sup>4</sup>Laboratoire Magmas et Volcans, Université Blaise Pascal, Clermont-Ferrand, France

**Abstract** Volcanic plumes from Etna volcano (Italy) are governed by easterly winds driving ash over the Ionian Sea. The limited land tephra deposit makes total grain-size distribution (TGSD) assessment and its fine ash fraction highly uncertain. On 23 February 2013, a lava fountain produced a ~9-km-high column above sea level (a.s.l.). The atypical north-easterly wind direction dispersed the tephra from Etna to the Puglia region (southern Italy) allowing sampling up to very distal areas. This study uses field measurements to estimate the field-based TGSD. Very fine ash distribution (particle matter below 10  $\mu\text{m}$ —PM<sub>10</sub>) is explored parameterizing the field-TGSD through a bi-lognormal and bi-Weibull distribution. However, none of the two latter TGSDs allow simulating any far-traveling airborne ash up to distal areas. Accounting for the airborne ash retrieved from satellite (Spinning Enhanced Visible and Infrared Imager), we proposed an empirical modification of the field-based TGSD including very fine ash through a power law decay of the distribution. The input source parameters are inverted by comparing simulations against measurements. Results suggest a column height of ~8.7 km a.s.l., a total erupted mass of  $\sim 4.9 \times 10^9$  kg, a PM<sub>10</sub> content between 0.4 and 1.3 wt%, and an aggregate fraction of ~2 wt% of the fine ash. Aerosol optical depth measurements from the AEROSOL ROBOTIC NETWORK are also used to corroborate the results at ~1,700 km from the source. Integrating numerical models with field, ground-based, and satellite-based data aims at providing a better TGSD estimation including very fine ash, crucial for air traffic safety.

**Plain Language Summary** On 23 February 2013, an intense lava fountain at Etna volcano, Italy, produced a ~9-km-high volcanic plume. The effect of a south-westerly winds dispersed the erupted material (tephra) from Etna to the Puglia region (~410 km from the source; southern Italy). These conditions permitted tephra sampling from the volcano up to Puglia. Field data are used to assess the total grain-size distribution (TGSD) to feed the FALL3D tephra dispersal model to reconstruct the tephra loading and airborne ash dispersal. To account for satellite data, we modified the TGSD adding the missing very fine ash content. Best simulations were selected by comparing computed and observed measurements in terms of tephra loadings and airborne ash mass. Results give an eruptive column height of ~8.7 km a.s.l., a total erupted mass of  $\sim 4.9 \times 10^9$  kg, a very fine ash content between 0.4 and 1.3 wt%, and an aggregated ash fraction of ~2 wt% of the fine ash. Results are also compared with aerosol measurements. Integrating numerical models with field and satellite-based data aims at providing a better TGSD estimation including the very fine ash fraction (below 0.01 mm), crucial for air traffic safety.

### 1. Introduction

One of the main goals of modern volcanology is a better understanding and quantification of eruption source parameters (ESP) governing tephra dispersal during a volcanic crisis. This is done using field (e.g., Andronico, Cristaldi, et al., 2008; Andronico, Scollo, et al., 2008; Andronico, Scollo, Lo Castro, et al., 2014), remote-sensing retrievals (e.g., Corradini et al., 2008, 2016; Gouhier et al., 2016; Scollo et al., 2012, 2014), laboratory experiments (e.g., Bagheri & Bonadonna, 2016; Cigala et al., 2017; Mueller, Ayris, et al., 2017; Mueller, Kueppers, et al., 2017), and numerical models (e.g., Bonadonna & Costa, 2012; Folch et al., 2016; Scollo et al., 2008). ESP assessment (e.g., Folch, 2012; Mastin et al., 2009) involves the estimation, among others, of the mass eruption rate (MER), which combined with the eruption duration provides the total erupted mass (TEM). The field-derived TEM is obtained by integrating the isomass maps (e.g., Bonadonna & Costa, 2013), which requires tephra deposits to be sampled at several locations (Bonadonna et al., 2015). In addition to the

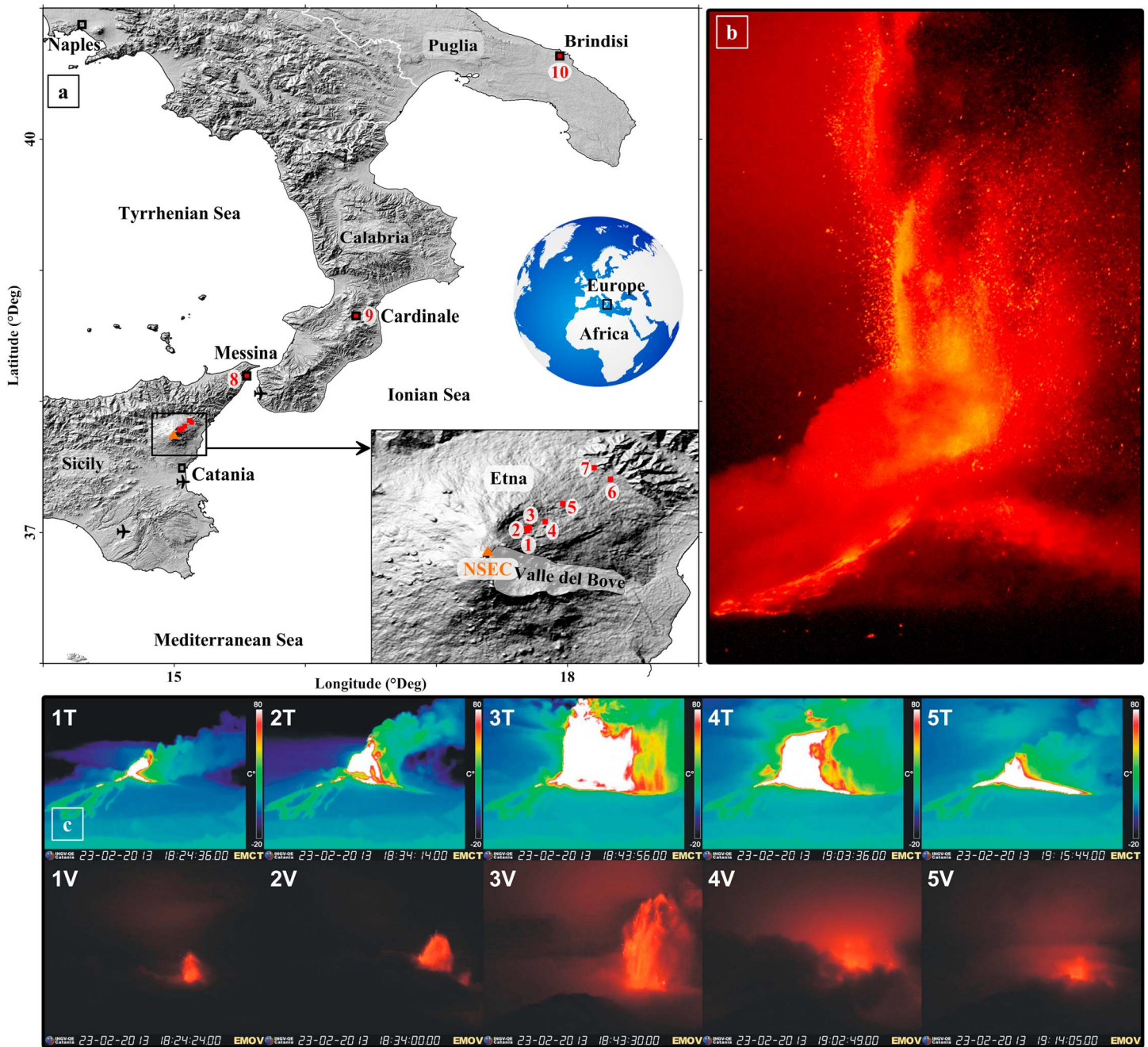


**Figure 1.** (a) The Italian regions (i.e., Sicily, Calabria and Puglia) affected by tephra fallout of the 23 February 2013 Etna paroxysm. NSEC stands for New Southeast Crater from which the eruption occurred. Red numbers refer to the sample sites, whereas the aircraft symbols localize the Fontanarossa (Catania), the Pio La Torre (Sicily), and the Tito Minniti (Calabria) airports. The inset zooms on Etna indicate the proximal samples (details in Table 1). (b) Photograph of the eruption. Courtesy of Marco Neri. (c) Time series pictures of the eruption in thermal (1–5 T) and visible (1–5 V) spectrum. Source: INGV-OE.

TEM, field data give geolocalized grain-size distributions (GSD) permitting the total grain-size distribution (TGSD) to be estimated by integrating local GSD (Bonadonna et al., 2015; Bonadonna & Houghton, 2005). Tephra is classified depending on the size (e.g., Folch, 2012), as bombs or blocks (i.e., diameter— $d \geq 64$  mm), lapilli ( $2 \leq d < 64$  mm), and ash ( $d < 2$  mm). Within ash, we further distinguish fine ash ( $d < 1$  mm), very fine ash ( $d < 30 \mu\text{m}$ ; Rose & Durant, 2009), and ultra-fine ash ( $d < 5 \mu\text{m}$ ). Hereinafter, we define the very fine ash as particle matter below  $10 \mu\text{m}$  (hereinafter  $\text{PM}_{10}$ ). Nonetheless, the TGSD strongly depends on the sampling distance from the source (Costa, Pioli, et al., 2016), the number of available

**Table 1**  
List of the Collected Samples With Their Numerical Results for Each Input Total Grain-Size Distribution (TGSD)

Sample	Field observations					Computed loading (kg/m <sup>2</sup> )			
	Location	Longitude	Latitude	Mode (Φ)	Loading (kg/m <sup>2</sup> )	Field TGSD	Bi-Gaussian TGSD	Bi-Weibull TGSD	Fine Enriched TGSD
1	Baracca	15.042	37.782	-3.5	$2.1 \times 10^1$	$4.5 \times 10^0$	$7.6 \times 10^0$	$6.5 \times 10^0$	$4.5 \times 10^0$
2	Casetta	15.041	37.784	-4.0	$5.9 \times 10^0$	$4.5 \times 10^0$	$7.7 \times 10^0$	$6.6 \times 10^0$	$4.6 \times 10^0$
3	Bivio-007	15.044	37.786	-4.0	$5.5 \times 10^0$	$4.7 \times 10^0$	$7.9 \times 10^0$	$6.8 \times 10^0$	$4.7 \times 10^0$
4	Forestale	15.061	37.792	-3.5	$2.2 \times 10^1$	$5.1 \times 10^0$	$8.5 \times 10^0$	$7.3 \times 10^0$	$5.1 \times 10^0$
5	Chalet	15.081	37.813	-2.5	$3.2 \times 10^1$	$6.1 \times 10^0$	$9.6 \times 10^0$	$8.4 \times 10^0$	$6.1 \times 10^0$
6	Castiglione	15.114	37.854	-1.5	$5.2 \times 10^0$	$8.0 \times 10^0$	$1.1 \times 10^1$	$9.5 \times 10^0$	$8.1 \times 10^0$
7	Linguaglossa Out	15.133	37.840	-3.0	$1.2 \times 10^0$	$8.4 \times 10^0$	$1.1 \times 10^1$	$1.0 \times 10^1$	$8.5 \times 10^0$
8	Messina	15.554	38.195	1.0	$2.9 \times 10^{-1}$	$1.2 \times 10^0$	$1.1 \times 10^0$	$9.4 \times 10^{-1}$	$1.3 \times 10^0$
9	Cardinale	16.384	38.650	2.0	$1.3 \times 10^{-2}$	$3.9 \times 10^{-2}$	$2.0 \times 10^{-2}$	$2.2 \times 10^{-2}$	$4.0 \times 10^{-2}$
10	Brindisi	17.941	40.634	3.0	$1.4 \times 10^{-3}$	$1.8 \times 10^{-3}$	$1.5 \times 10^{-4}$	$5.4 \times 10^{-4}$	$1.8 \times 10^{-3}$

Note. Sampling includes locations, tephra loadings, and modes. The computed loadings result from the use of the Field, bi-Gaussian, bi-Weibull, and Fine Enriched TGSDs (Figure 4).

samples (Bonadonna et al., 2015; Bonadonna & Houghton, 2005), and the spatial distribution (Bonadonna et al., 2015; Spanu et al., 2016). Moreover, the fine ash fraction within the TGSD is likely underestimated due to the long atmospheric residence time ranging from hours to days (Rose & Durant, 2009), preventing very fine ash from sampling at reasonable distance (Costa, Pioli, et al., 2016). For these reasons, TGSD assessment is highly uncertain, especially for the fine ash fraction (Bonadonna et al., 2011; Costa, Pioli, et al., 2016), which depends on the eruption type (Rose & Durant, 2009). Indeed, a basaltic volcano commonly produces a fine ash fraction of a few percent of the erupted material, whereas the fraction from silicic eruption contains between 30% and 50% (Rose & Durant, 2009).

The statements described above highlight the need for an integrated approach that encompasses the grain-size spectrum down to the very fine ash. Recent eruptions reveal how an accurate estimation of such fraction is crucial for air traffic safety (e.g., Bonadonna et al., 2011; Casadevall, 1994; Folch et al., 2012). As an example, Bonadonna et al. (2011) integrated field and satellite information to better characterize the TGSD of the May 2010 Eyjafjallajökull eruption, which had a relatively large very fine ash population (Costa, Pioli, et al., 2016). Motivated by their results, we aim at reconstructing the entire TGSD (including PM<sub>10</sub>), integrating field measurements and satellite-based observations of the 23 February 2013 Etna paroxysm.

At Etna, more than 200 lava fountains occurred from the New Southeast Crater (NSEC) between 1995 and 2014 (Andronico, Scollo, Lo Castro, et al., 2014; De Beni et al., 2015; Corsaro et al., 2017). Most eruption columns reached several kilometers high releasing ash into the atmosphere. The prevailing easterly winds over the Etnean region (Barsotti et al., 2010; Scollo et al., 2013) dispersed the tephra downwind over the Ionian Sea. Consequently, the narrow land surface (i.e., 5–20 km eastward from source) affects the sampling area and, therefore, the field-derived TGSD. Andronico, Scollo, Cristaldi, et al. (2014) demonstrated how an incomplete field data set for Etna (e.g., location and spatial distribution) influences the TGSD estimation and the TEM retrieval. In addition, Azzopardi et al. (2013) showed that an incorrect ESP assessment may also impact the forecast of the plume transport over neighboring countries, such as the Maltese Islands.

On 23 February 2013, the eruption dispersed tephra fallout north-eastward permitting sampling from the proximal volcanic slopes to Brindisi (Puglia region) about 410 km from the source (Figure 1 and Table 1). In the literature, only a few studies on Etna eruptions used similar distal field observations (Dellino & Kyriakopoulos, 2003), but the paucity of data prevented using within the TGSD calculation. Here, starting from the field-derived TGSD for the 23 February 2013 paroxysm, we inverted the PM<sub>10</sub> fraction required within the TGSD for numerically reconstructing simultaneously the tephra loading and far-traveling airborne ash mass. Simulations were run coupling FPlume (Folch et al., 2016) with the FALL3D tephra dispersal model (Costa et al., 2006; Folch et al., 2009). Simulation input parameters (ESP) were inverted by best-reproducing field and satellite retrievals.

Worldwide high time-resolution satellite coverage allows most eruptive processes to be recorded (Gouhier et al., 2016). Geostationary platforms, such as meteorological second generation, are particularly suited to rapidly evolving volcanic plume observations (Prata & Kerkmann, 2007) with an acquisition frequency of up to one image every 5 min with the rapid scan service. In addition to satellite data, the ground-based Aerosol RObotic NETwork (AERONET) is used to validate the satellite retrievals and simulations of ultra-fine particles (i.e., few micrometers; Folch et al., 2012). Although combining data from different instruments is challenging due to their own operative window, this work aims to show that an integrated multidisciplinary approach is necessary for better assessing the TGSD, which is pivotal for air traffic safety (e.g., Beckett et al., 2015; Folch et al., 2012). Indeed, improving ash plume characterization in terms of ash concentration and dispersion is highly relevant for the volcanic ash advisory centers (VAACs) and the pilots to prevent ash encounters. As testified by several cases worldwide in the last 30 years (Casadevall, 1994; Casadevall et al., 1999; Grindle & Burcham, 2003; Guffanti et al., 2005; Prata, 1989a), the data can be used for delimiting the no-fly zones, helping the decision makers, such as those working in the VAACs. Considering that there is no operational single method capable of describing fully the volcanic eruption processes, tracking the plume, and assessing the ESPs, their estimation can only be obtained through a synergistic integrated approach.

To provide alerts of volcanic activity in support of air traffic safety, the nine VAACs use operational volcanic ash transport and dispersion models, such as (1) the Numerical Atmospheric-dispersion Modeling Environment (NAME; Beckett et al., 2014; Witham et al., 2007) for the London VAAC, (2) the “MODèle de Chimie Atmosphérique à Grande Echelle” (MOCAGE-accident; Sič et al., 2015) for the Toulouse VAAC, and (3) the FALL3D for the Buenos Aires and Darwin VAACs. However, their initializations commonly use simplified TGSD. For example, NAME assumes a standard grain-size distribution from a preexisting eruption (Maryon et al., 1999), arbitrarily considering 5% in weight of the TEM for the fine ash content.

Besides the aviation hazard, volcanic ash also affects populations living near active volcanoes (e.g., Sulpizio et al., 2012). In particular, PM<sub>10</sub> has respiratory health effects even for eruptions produced by Etna (e.g., Andronico & Del Carlo, 2016; Horwell, 2007; Horwell et al., 2013, 2017; Rose & Durant, 2009; Tomašek et al., 2016).

The paper describes, first, the 23 February 2013 eruption features. Then, the modeling approach is followed by the methodology used to reconstruct the TGSD and assess the best ESPs. We report the different data set used (i.e., field, satellite, and ground based) prior to presenting and discussing the results.

## 2. Chronology of the 23 February 2013 Eruption

On 23 February 2013, an intense lava fountain took place at the NSEC (Figure 1b), which is the youngest and most active of Etna's craters (Andronico et al., 2015; Behncke et al., 2014). The eruptive activity initiated with Strombolian explosions, which increased around 18:15 UTC turning into lava fountaining (Figure 1c). The paroxysmal phase lasted 1 hr and 6 min. Despite bad weather conditions (i.e., cloudy, windy, and night) during the paroxysmal activity, images from the “Istituto Nazionale di Geofisica e Vulcanologia—Osservatorio Etno” (INGV-OE) showed the growth of incandescent lava jets higher than 500 m above the crater (Figures 1b and 1c), from which a buoyant plume developed up to ~9 km above sea level (a.s.l.) forming the umbrella region. Figure 2 shows the main meteorological profiles (e.g., temperature, air moisture, wind speed, and direction) obtained from the European Center for Medium-range Weather Forecasts (ERA-Interim-Reanalysis). Considering the time for the ash to be transported from NSEC to Brindisi (i.e., ~5 h), the two profiles refer to 18:30 UTC and 23:30 UTC, respectively. This study benefited from atypical meteorological conditions in wind speed and direction during the eruption and the following hours, with similar patterns over NSEC and Brindisi. Indeed, the wind speed at 18:30 UTC and 8.5 km a.s.l. is ~49.6 and ~32.6 m/s over NSEC and Brindisi, respectively, whereas at 23:30 UTC, it is ~50.6 and ~36.3 m/s. Such a context made sampling possible from Etna's slopes (5–16 km from the source) to Messina (~70 km) up to Calabria and Puglia regions (~160 and ~410 km, respectively). Field location and data are available in Figure 1 and Table 1, respectively.

In the deposit, we found lapilli up to 5–6 km from the vent (samples 1–7), coarse ash (i.e., 2–0.125 mm) in Messina (sample 8), fine ash with mode at 0.25 mm in Cardinale (sample 9), and the finest ash deposit in Brindisi (sample 10) with mode around 0.125 mm (details in Table 1). Geochemical analysis on several samples indicate a CaO/Al<sub>2</sub>O<sub>3</sub> ratio in glass (Corsaro & Miraglia, 2013a), suggesting slightly different compositions

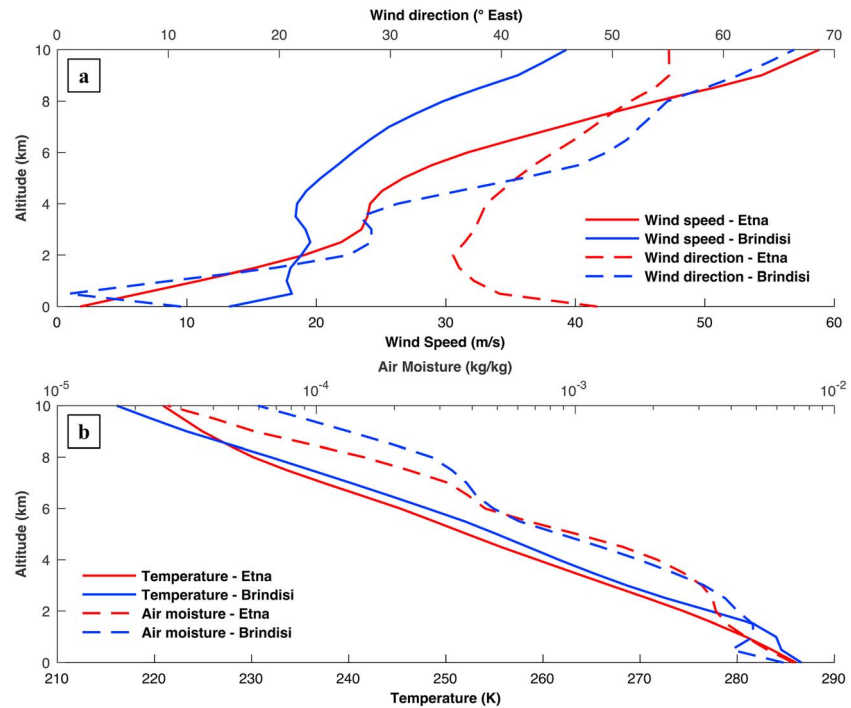


**Figure 2.** (a) Wind direction and speed profiles above the New Southeast Crater and Brindisi at 18:30 UTC and 23:30 UTC, respectively. (b) Associated air moisture and temperature profiles. Data refer to the 23 February 2013, which are provided by the European Center for Medium-range Weather Forecasts platform (ERA-Interim-Reanalysis).

from those measured during the 2011–2012 sequence (Behncke et al., 2014). They also show more evolved magma than on the 23 November 2013 (Andronico et al., 2015; Corsaro & Miraglia, 2013b).

### 3. Modeling Approach: FPlume and FALL3D Models

Tephra dispersal models are widely used in volcanology to quantify either the tephra loading (e.g., TEPHRA, Connor et al., 2001; HAZMAP, Macedonio et al., 2005; FALL3D, Costa et al., 2006; Folch et al., 2009) or the airborne volcanic ash (e.g., VOL-CALPUFF, Barsotti et al., 2008; FALL3D). All tephra dispersal models need input parameterizations of the source term (e.g., eruptive column, MER, TGSD). An overview of such models is available in Folch (2012) and Costa, Suzuki, et al. (2016).

This study uses FALL3D to compute the tephra dispersal and sedimentation by means of FPlume (Folch et al., 2016), which is a steady-state eruption column model based on the buoyant plume theory (Morton et al., 1956). FPlume solves for one-dimensional cross-section-averaged equations for mass, momentum, and energy conservations, accounting for the effects of wind coupling, air moisture, particle re-entrainment, and ash aggregation under wet conditions. Within FALL3D, FPlume uses the TGSD together with the initial magma temperature and water content to provide the vertical particle distribution inside the column. Etna is a basaltic volcano producing magmas typically at 1,300 K with ~2.5 wt% of magmatic water (Allard et al., 2005; Carbone et al., 2015; Metrich et al., 2004; Metrich & Rutherford, 1998; Spilliaert et al., 2006). FPlume estimates the MER for a column height and a given wind profile by using two turbulent air entrainment coefficients (i.e., radial ( $\alpha$ ) and cross-flow ( $\beta$ ) coefficients; Bursik, 2001; Suzuki & Koyaguchi, 2015).  $\alpha$  is internally calculated (details in Kaminski et al., 2005; Folch et al., 2016), whereas  $\beta$  is poorly constrained (Costa, Suzuki, et al., 2016), being calibrated based on best-fitting the field measurements. Characterizing the source term through FPlume implies uncertainties associated with the input parameters (see Macedonio et al., 2016).

The three-dimensional time-dependent Eulerian FALL3D model solves a set of advection-diffusion-sedimentation equations over a structured terrain-following grid using a finite difference method (Costa et al., 2006; Folch et al., 2009). Besides the ESPs, FALL3D requires the time-dependent meteorological fields across the computational domain (Figure 1). For the simulated period (i.e., from 00:00 UTC on 23 February

**Table 2**  
List of the Input Parameters for FPlume and FALL3D Modeling With Their Ranges

Parameter	Explored range	
Column height (km a.v.)	3	10
Mass Eruption Rate (kg/s)	$10^3$	$10^8$
Exit velocity (m/s)	150	300
Exit water fraction (%)	0.5	3.2
Cross-flow entrainment coefficient ( $\beta$ )	0.3	1.0
Aggregate diameter ( $\Phi_{\text{Agg}}$ )	1	2.5
Density aggregates ( $\text{kg/m}^3$ )	200	1,200

Note. Other options and models are described in Appendix A.

up to 00:00 UTC on 29 February 2013), European Center for Medium-range Weather Forecasts meteorological data were obtained every 6 h for 37 pressure levels (i.e., from 1,000 to 1 mb) at  $0.75^\circ$  horizontal resolution. It is worth noting that the resolution is too low for capturing the orographic effects, which can be very important at local scale (e.g., around Etna's slopes), affecting the tephra loading (Watt et al., 2015). FALL3D uses an internal meteorological grid interpolated here at 4-km resolution (the grid mesh is displayed in Figure S1 in the supporting information). Although gravity currents in the umbrella region are not significant for such a small eruption (Costa et al., 2013), the simulations accounted for these effects. Ash aggregation, assumed negligible in terms of mass, was also investigated following a scheme based on a simplified solution of the Smoluchowski equation (Smoluchowski, 1917) proposed by Costa et al. (2010). Aggregation scheme uses a fractal relationship of the number of primary particles within an aggregate together with the effects of both

magmatic water and air moisture (Folch et al., 2010, 2016). Further description of the models and the parameterizations used for ash aggregation are available in Poret et al. (2017).

## 4. Observational Data and Methodology

The methodology proposed here brings together field and satellite data to reconstruct the initial grain-size distribution in the plume before sedimentation (i.e., input TGSD). A summary of the input parameters is available in Table 2. As first step, we used the field samples to retrieve the TGSD. Then, the TGSD was parameterized using lognormal and Weibull distributions (Costa, Pioli, et al., 2016, 2017). ESPs were inverted by capturing the measurements. Finally, the field-based TGSD was extrapolated for implementing the very fine ash distribution through an analytical parameterization. Satellite retrievals were used to invert the  $\text{PM}_{10}$  fraction by best-fitting the simulated distal airborne ash mass. We also validated the results by analyzing the ultra-fine ash dispersal with the AERONET data.

### 4.1. Field Data Analysis

In volcanology, the particle-size spectrum is typically expressed in  $\Phi$ -units through the relationship  $d = 2^{-\Phi}$ , with the diameter  $d$  in millimeters (Krumbein, 1934). Few hours after the eruption, tephra was sampled at 10 different locations (Figure 1). Prior to analysis, loading per unit area was measured, and samples were oven-dried at  $110^\circ\text{C}$  for 12 hr at the sedimentology laboratory of the INGV-OE. Then, GSD was retrieved from  $-5$  to  $5 \Phi$  (at  $0.5 \Phi$  interval) by sieving (via a Retsch vibratory sieve shaker AS 200 Basic). The farthest sample (i.e., no. 10 in Figure 1) contains only small fine ash (i.e.,  $d \geq 2 \Phi$ ), preventing sieve analysis. The GSD was given by the CAMSIZER (Retsch) instrument, which has the same range size limit as the sieve (Lo Castro & Andronico, 2008). Andronico, Scollo, Cristaldi, et al. (2014) validated their alternative use showing the good match between the two methods above for grain-size analysis purpose. The field GSDs indicate a clear decay in size from proximal to distal areas and an increase in tephra sorting with distance (Figure 3). They also show unimodal behavior, peaking at  $-4 \Phi$  for medial locations and  $3 \Phi$  for the distal ones (Table 1).

Beside GSD, we used the field data to estimate the total mass of the deposit using the method of Bonadonna and Costa (2012, 2013), which is based on the Weibull distribution of the deposit thinning. The resulting field-derived TEM estimate yields  $\sim 2.0 \pm 0.5 \times 10^9$  kg.

### 4.2. Satellite Data (Spinning Enhanced Visible and Infrared Imager)

Satellite-based thermal infrared sensors are very useful for characterizing volcanic ash (Gouhier et al., 2016; Guéhenneux et al., 2015). In the thermal infrared region (i.e.,  $7\text{--}14 \mu\text{m}$ ), we can distinguish silicate particles (e.g., volcanic ash) from other aerosols (e.g., ice crystals,  $\text{SO}_2$ , or  $\text{H}_2\text{SO}_4$ ) using a two-channel difference model based on the absorption feature between the  $11\text{-}$  and  $12\text{-}\mu\text{m}$  wavelengths (Prata, 1989b; Watson et al., 2004; Wen & Rose, 1994). It was shown that the difference between the at-sensor "Planck" brightness temperature (referred to as BT) observed in these two channels is negative ( $-\Delta T$ ) for ash and positive ( $+\Delta T$ ) for ice. Wen and Rose (1994), built on early work (Prata, 1989b), developed a forward retrieval model that quantifies the effective radius ( $r_e$ ) and optical depth ( $\tau_c$ ) from the extinction efficiency factor ( $Q_{\text{ext}}$ ) calculated using the

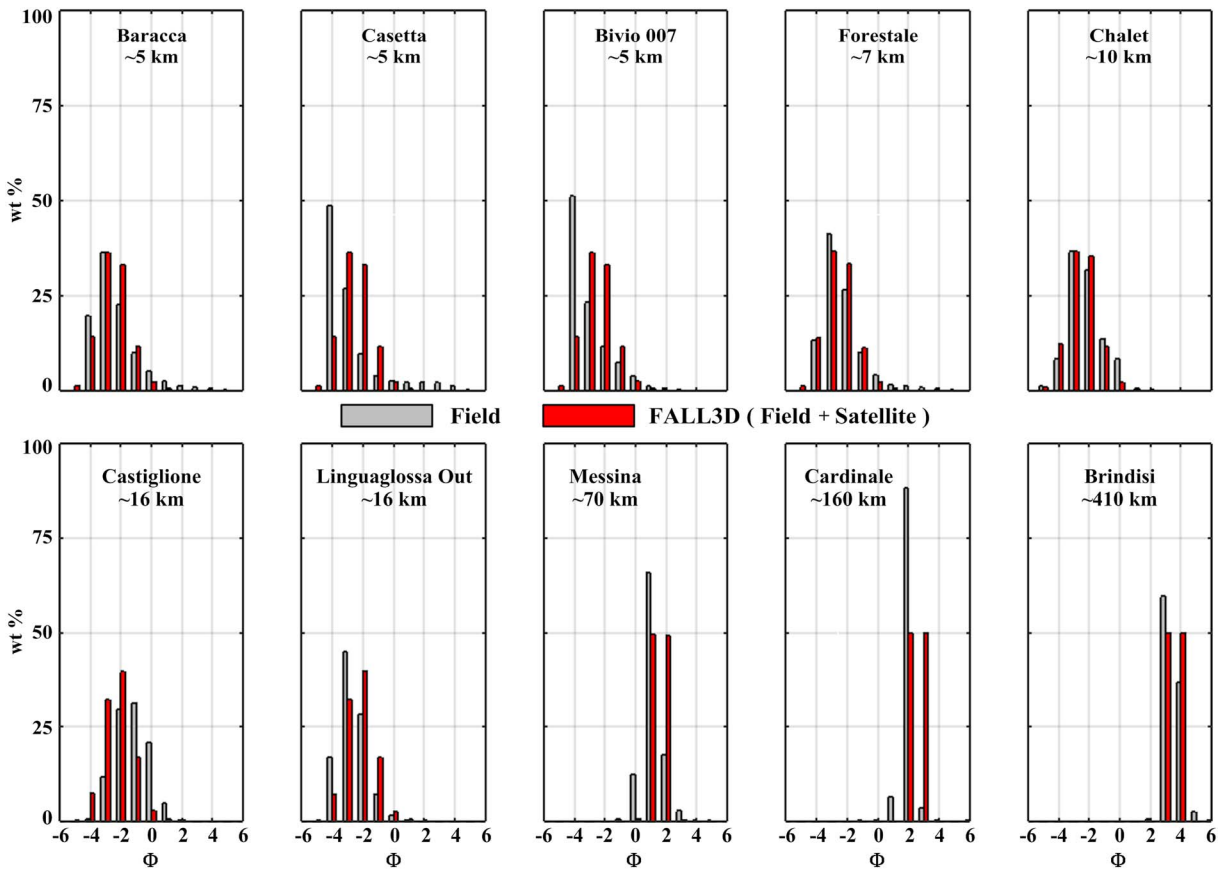


**Figure 3.** Individual field grain-size distribution of the 10 samples together with the ones computed by considering both field and satellite observations (i.e., Fine Enriched total grain-size distribution).

Mie theory. This allows a theoretical lookup table to be produced for sets of variations of both  $r_e$  and  $\tau_c$  as a function of the brightness temperature. From the inverse procedure,  $r_e$  and  $\tau_c$  (and hence the mass of the volcanic ash cloud) can be retrieved for any given brightness temperature pair (details in Prata & Grant, 2001; Watson et al., 2004). However, satellite retrievals are affected by several factors such as the surface characteristics (i.e., temperature and emissivity), plume geometry (i.e., altitude and thickness), ash optical properties, and water vapor. These factors produce an uncertainty of  $\sim 40\%$  and  $\sim 30\%$  respectively associated with the total mass retrieval and effective radius (Corradini et al., 2008). Another source of uncertainty is related to the presence of relatively large particles (typically for  $r_e > 6 \mu\text{m}$ ), possibly within the fine ash clouds, which cannot be retrieved using the Mie theory as  $Q_{\text{ext}}$  does not vary significantly for  $r_e > \lambda/2$  (Guéhenneux et al., 2015; Stevenson et al., 2015). Overall, the effects related to both misdetection issues (i.e., BTD) and the presence of coarse ash particles in the cloud lead to a mass underestimation of 50% (Stevenson et al., 2015).

We used data from the Spinning Enhanced Visible and Infrared Imager (SEVIRI) sensor onboard Meteosat-10, which provides images every 15 min at a spatial resolution of  $\sim 3 \times 3 \text{ km}$  at nadir. Satellite data were acquired from HOTVOLC (<http://hotvolc.opgc.fr>), a web-based satellite-data-driven monitoring system developed at the Observatoire de Physique du Globe de Clermont-Ferrand (France). The system is designed for real-time monitoring of active volcanoes (Gouhier et al., 2016). During the 23 February 2013 Etna eruption, the volcanic cloud was tracked in the SEVIRI data in terms of airborne ash mass (hereinafter AAM; in kilograms) over hundreds of kilometers. SEVIRI level 1.5 data recorded by the HOTVOLC system were initially converted into calibrated spectral radiance (in  $\text{W m}^{-2}\text{sr}^{-1} \mu\text{m}^{-1}$ ). Then, following the methodology described above (Guéhenneux et al., 2015; Wen & Rose, 1994), we provide the cloud top temperature ( $^{\circ}\text{C}$ ), altitude (m a.s.l.), AAM (kg), and  $r_e$  ( $\mu\text{m}$ ) from 19:00 to 20:15 UTC.

### 4.3. AERONET Data

The AERONET is a ground-based remote sensing network (Holben et al., 1998) supervised by the National Aeronautics and Space Administration (NASA) and the Photométrie pour le Traitement Opérationnel de Normalisation Satellitaire. AERONET aims at retrieving in real time a global database from solar spectral irradiance to assess aerosol optical properties, for example, volume size distribution, particle sphericity (estimated here as the ratio between the backscattered and the depolarization signals), and aerosol optical depth (AOD) to validate satellite observations (Dubovik et al., 2006). The columnar AOD is measured from solar radiance (Holben et al., 2006) at diverse spectral channels (e.g., 500 nm) through three data quality levels (Dubovik et al., 2006). In addition, direct-sun-derived AOD processing (O'Neill et al., 2003; Watson & Oppenheimer, 2001) integrates signal (in voltage) from the sensor to the top of the atmosphere, given by the sun-photometer measurement at the Mauna Loa Observatory of Hawaii. The proportionality between the spectral irradiance at the sensor and the acquired signal is used to convert into AOD. However, wavelength-dependent gas (e.g., H<sub>2</sub>O, O<sub>3</sub>, NO<sub>2</sub>, CO<sub>2</sub>, and CH<sub>4</sub>) may scatter light and must be subtracted when calculating the AOD. During the inversion procedure, the error is assumed to be distributed lognormally and uncorrelated giving a standard deviation of 5% associated with the sky radiance measurement (Dubovik, 2004; Dubovik et al., 2000; Dubovik & King, 2000). AOD at 500-nm wavelength is used as standard to compute the fine mode fraction of the total AOD (e.g., Folch et al., 2012). It is worth noting that the assumption of a lognormal distribution, made for both AERONET and satellite retrievals, is not fully consistent with the empirical distribution we adopt in this work and has to be considered as an approximation of it.

The 23 February 2013 Etna paroxysm released very fine ash toward south-eastern Europe. Among the AERONET sites, the station located at Çamlıbel, Turkey (station labeled IMS-METU ERDEMLI, ~1,700 km from Etna) detected particles from 24–26 February 2013. Unfortunately, the eruptive period overlapped with a substantial resuspension of Saharan dust from 20 to 23 February 2013. Even though the dust storm was in a final stage, the presence of airborne mineral dust affected the AOD retrieved over the station. To assess the volcanic ash AOD, we subtracted the dust contribution estimated from the Goddard Earth observing system (GEOS-chem) model (Bey et al., 2001; Chan & Chan, 2017; Fairlie et al., 2007; Park et al., 2004). Although such approach introduces a large uncertainty in the retrieval, we bear in mind that data were used to validate the satellite observations only by verifying if the input TGSD permits the reproduction of the ultrafine ash dispersal at ~1,700 km from the source. Indeed, we compared the computed volcanic ash AOD (FALL3D) with the AERONET measurements.

### 4.4. TGSD Estimation

Making use of the 10 field GSDs, the field-derived TGSD (hereinafter Field TGSD; Figure 4) is estimated through the Voronoi tessellation method (Bonadonna & Houghton, 2005). Regarding the spatial distribution of the samples, the Field TGSD suffers from the lack of field data, especially at medial and distal locations. Consequently, it cannot fully represent the initial magma fragmentation but only an estimation with, for the first time on Etna, medial and distal measurements. Figure 4a shows the bimodality of the Field TGSD with a first mode (i.e., the coarse sub-population) around  $-3 \Phi$  and a second mode (i.e., the fine sub-population) around  $0.5 \Phi$ . To reproduce the Field TGSD in a simple parametric way and extrapolate to the very fine ash fraction, we describe the TGSD as the sum of two lognormal distributions (bi-Gaussian in  $\Phi$ , hereinafter bi-Gaussian distribution), and two Weibull distributions (hereinafter bi-Weibull distribution). The bi-Gaussian distribution was constructed following the equation (Costa, Pioli, et al., 2016):

$$f_{\text{bi-Gaussian}}(\Phi) = p \frac{1}{\sigma_1 \sqrt{2\pi}} e^{-\frac{(\Phi-\mu_1)^2}{2\sigma_1^2}} + (1-p) \frac{1}{\sigma_2 \sqrt{2\pi}} e^{-\frac{(\Phi-\mu_2)^2}{2\sigma_2^2}} \quad (1)$$

where  $\Phi$  is the particle diameter in logarithmic scale,  $p$  and  $(1-p)$  are the fractions of each subpopulation, and  $\mu_1, \mu_2, \sigma_1,$  and  $\sigma_2$  (Table 3) are the mean and standard deviations of the two Gaussian distributions in  $\Phi$ -units, respectively (Figure 4a). The cases well characterized in terms of fine ash fraction indicate that a lognormal distribution tends to underestimate the fine ash distribution (Costa, Pioli, et al., 2016). This becomes significant for TGSD produced by Etna eruptions, as most of the fine ash is typically not sampled. In the latter



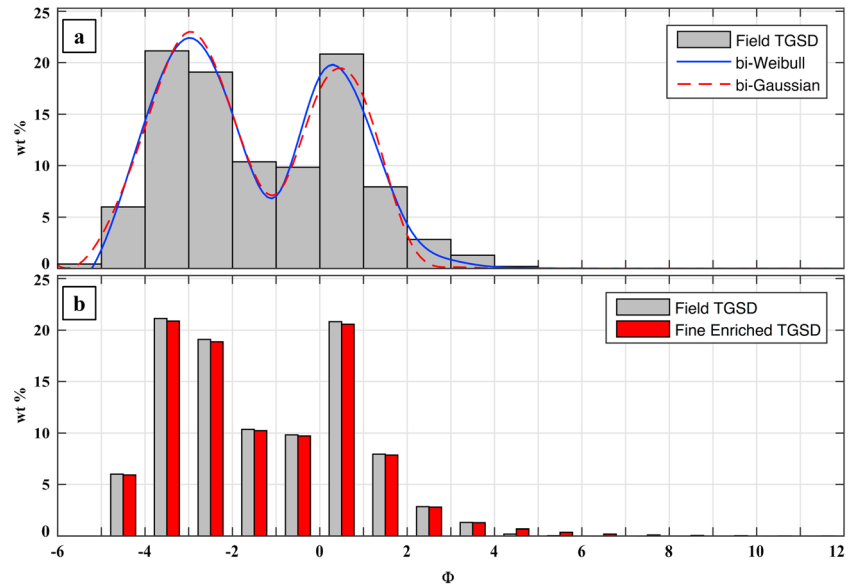


**Figure 4.** Summary of the input total grain-size distributions (TGSDs) used within the simulations. (a) Field TGSD together with its best-fitting analytical curves (bi-Gaussian and bi-Weibull distributions; details in Table 3). (b) Fine Enriched TGSD obtained from the Field TGSD by modifying empirically the fine ash distribution.

case, Costa, Pioli, et al. (2016, 2017) demonstrated that a better quantification of the fine ash fraction is given by the bi-Weibull distribution as follows:

$$f_{\text{bi-Weibull}}(d) = q \frac{1}{n_1^{\frac{1}{n_1}} \Gamma\left(1 + \frac{1}{n_1}\right)} \frac{1}{\lambda_1} \left[\frac{d}{\lambda_1}\right]^{n_1} e^{-\left(\frac{d}{\lambda_1}\right)^{n_1}} + (1 - q) \frac{1}{n_2^{\frac{1}{n_2}} \Gamma\left(1 + \frac{1}{n_2}\right)} \frac{1}{\lambda_2} \left[\frac{d}{\lambda_2}\right]^{n_2} e^{-\left(\frac{d}{\lambda_2}\right)^{n_2}} \quad (2)$$

where  $q$  and  $(1 - q)$  are the fractions of each subpopulation and  $\lambda_1, \lambda_2, n_1,$  and  $n_2$  (Table 3) represent the scale and shape parameters of the two distributions, respectively (Figure 4a).

Neither the Field TGSD, the bi-Gaussian, nor the bi-Weibull distributions (Figure 4) permit to capture numerically the satellite retrievals. We assume that this is due to the missing information relative to the very fine ash ( $\text{PM}_{10}$ , i.e.,  $\Phi \geq 6$ ) or the lognormal shape given to the partial GSD into the satellite data. Indeed, the long atmospheric residence time of the  $\text{PM}_{10}$ , for negligible ash aggregation, prevents a rapid deposition (Rose & Durant, 2009). To account for  $\text{PM}_{10}$  within the TGSD, without accurate satellite-derived GSD, we opted for an empirical modification of the Field TGSD to enrich in fines the corresponding classes (i.e.,  $\Phi \geq 5$ ; Figure 4b).

Indeed, we assume that for a limited range within the TGSD (i.e.,  $\text{PM}_{10}$ ), the lognormal distribution can approximate the empirical distribution we used for characterizing the  $\text{PM}_{10}$ . For the sake of simplicity, we used an empirical power law dependence of the fraction with  $\Phi$  according to the following relationship (Poret et al., 2018):

$$X(\Phi_i) = X(\Phi_4) \times \gamma^{(\Phi_i - \Phi_4)}, \quad \Phi \geq 5 \quad (3)$$

where  $X(\Phi_i)$  is the fraction (in weight %) allocated to the  $i$ th bin,  $X(\Phi_4)$  is the fraction obtained for  $\Phi = 4$ , and  $\gamma$  is the empirical factor ( $\gamma < 1$ ). Although  $\text{PM}_{10}$  refers to  $\Phi \geq 6$ , the Field TGSD does not permit calculating from  $\Phi = 5$  implying to start at  $\Phi = 4$  (see Figure 4b). The  $\text{PM}_{10}$  fraction required into the TGSD was inverted exploring  $\gamma$  between 0.5 and 0.7, which corresponds to a  $\text{PM}_{10}$  fraction of 0.3–1.3%. This empirical procedure aims at proposing the input TGSD (hereinafter Fine Enriched TGSD;

**Table 3**

Parameterization of the Analytical Distributions Obtained in Best Fit of the Field Total Grain-Size Distribution

Bi-Gaussian distribution		Bi-Weibull distribution	
$\mu_1$	$-2.96 \pm 0.07$	$\lambda_1$	$-3.28 \pm 2.84$
$\sigma_1$	$1.03 \pm 0.07$	$n_1$	$1.68 \pm 0.24$
$\mu_2$	$0.49 \pm 0.07$	$\lambda_2$	$-1.25 \pm 1.07$
$\sigma_2$	$0.79 \pm 0.06$	$n_2$	$0.77 \pm 0.16$
$p$	$0.59 \pm 0.03$	$q$	$0.39 \pm 0.06$

Note. Values are expressed in  $\Phi$ -units. The lognormal distribution is described through the coarse subpopulation fraction ( $p$ ), the means of the of coarse- and fine-grained subpopulations ( $\mu_1$  and  $\mu_2$ , respectively), and their standard deviations ( $\sigma_1$  and  $\sigma_2$ , respectively). The Weibull distribution is constructed with the coarse subpopulation fraction ( $q$ ), the scale parameters of the means of the coarse- and fine-grained subpopulations ( $\lambda_1$  and  $\lambda_2$ , respectively), and the shape parameters of the means of the coarse- and fine-grained subpopulations ( $n_1$  and  $n_2$ , respectively).

**Table 4**

Best Input Eruption Source Parameters and the Corresponding Statistical Analysis for the Tested Total Grain-Size Distributions (TGSDs)

Input parameter	Field TGSD	Bi-Gaussian TGSD	Bi-Weibull TGSD	Fine Enriched TGSD	
Column height (km a.v.)	5.5	5.5	5.5	5.5	5.5
Mass Eruption Rate (kg/s)	$1.2 \times 10^6$	$1.4 \times 10^6$	$1.3 \times 10^6$	$1.3 \times 10^6$	$1.3 \times 10^6$
Exit velocity (m/s)	250	250	250	250	250
Exit temperature (K)	1,300	1,300	1,300	1,300	1,300
Exit water fraction (%)	2.5	2.5	2.5	2.5	2.5
Cross-flow entrainment coefficient ( $\beta$ )	0.53	0.55	0.53	0.54	0.54
Diameter ( $\Phi_{Agg}$ )	—	—	—	—	2
Density aggregates (kg/m <sup>3</sup> )	—	—	—	—	1,000
Statistical metric					
$RMSE_1$	0.80	0.70	0.73	0.80	0.80
$RMSE_2$	2.28	2.84	2.46	2.31	2.31
$K$	1.00	1.01	0.99	0.99	0.99
$k$	3.36	3.58	2.96	3.37	3.37
Bias	0.0	0.0	0.0	0.0	0.0
Correlation	0.9	0.9	0.9	0.9	0.9
$t$ test	1.0	1.0	1.0	1.0	1.0

Note. Ash aggregation is investigated through the Fine Enriched TGSD using the scheme introduced in Costa et al. (2010).

Figure 4b) capable to account for both field and satellite data.  $\gamma$  is estimated by best-fitting the simulated AAM with the satellite retrievals.

#### 4.5. Inverse Problem-Solving Methodology

The inverse problem presented above is solved carrying out hundreds of simulations to explore the input parameter ranges (Table 2 and Appendix A for further parameterizations). Although more sophisticated Bayesian approaches can be used to deal with atmospheric observations (e.g., Rodgers, 2000; Twomey, 1996), the quantity and quality of the available data in terms of tephra loading and airborne ash mass motivated the inversion by means of simple statistical metrics as in similar studies (e.g., Costa et al., 2012, 2014; Folch et al., 2010; Martí et al., 2016; Poret et al., 2017). By means of the following analyses, we aim at suggesting a simple method for integrating the data and assessing the reflecting ESP. However, when the data make it possible, more sophisticated comparison can be used (e.g., Wilkins et al., 2016).

We initiated the inversion procedure by optimizing the simulations best-fitting the observed tephra loadings. For this purpose, we used a goodness-of-fit criterion evaluated through different statistical metrics (Poret et al., 2017). One was the normalized root mean square error (i.e.,  $RMSE$ ) calculated on the basis of two different weighting factors for the computed tephra loadings (i.e.,  $RMSE_1$  and  $RMSE_2$ ; equations and explanation in Appendix B). Besides  $RMSE$ , we measured the goodness-of-fit and uncertainty of the simulated tephra loadings through the statistical indexes  $K$  (i.e., geometric average of the distribution) and  $k$  (i.e., geometric standard deviation of the distribution) introduced by Aida (1978):

$$K = \exp \left[ \frac{1}{N} \sum_i^N \log \left( \frac{Obs_i}{Sim_i} \right) \right] \quad k = \exp \left[ \sqrt{\frac{1}{N} \sum_i^N \log \left( \frac{Obs_i}{Sim_i} \right)^2 - \left( \frac{1}{N} \sum_i^N \log \left( \frac{Obs_i}{Sim_i} \right) \right)^2} \right]$$

Making use of such criteria, the simulations are considered reliable when  $K$  lies between 0.95 and 1.05 (i.e.,  $\pm 5\%$  of the best theoretical mass estimation based on the sampled tephra loadings). In other words, a value of  $K = 0.95$  indicates a 5% overestimation of the TEM for a given set of ESPs, whereas  $K = 1.05$  gives an underestimation of 5%. The best simulations are selected when  $k$  is minimized. Additionally, we calculated also the bias (to be minimized), the correlation (to be maximized), and the Student  $t$  test (Folch et al., 2010; Poret et al., 2018).

To reproduce the tephra loading, we ran a set of simulations varying the parameters at constant steps within their ranges (Table 2). Then, we refined by means of a finer step around the best cases to optimize the goodness of fit. We started with the column height by changing the values from 6 to 13 km a.s.l. using the relationship between the column height and the MER (Folch et al., 2016). The latter was investigated iteratively

between  $10^3$  and  $10^8$  kg/s. Then, the exit velocity and the magma water content were explored from 150 to 300 m/s and 0.5 to 3.2%, respectively. Regarding the FPlume inputs to compute the air entrainment,  $\beta$  was sampled from 0.3 to 1.0. The aggregation parameterization was explored by considering the aggregate diameter ( $\Phi_{\text{Agg}}$ ) and density from 1 to 2.5  $\Phi$  and 200 to 1,200 kg/m<sup>3</sup>, respectively.

The methodology described above gives similar tephra loadings through diverse input combinations, which indicates non-uniqueness of the solution (Anderson & Segall, 2013; Bonasia et al., 2010; Connor & Connor, 2005; Scollo et al., 2008).

Regarding the satellite retrievals, the PM<sub>10</sub> fraction was inverted by quantitatively comparing the retrieved whole ash mass contained within the volcanic cloud (SEVIRI) with the simulated total AAM (in kg). We applied the same statistical method to the observed airborne PM<sub>10</sub> masses (section 4.4) than for field measurements.

## 5. Results

The following section describes the best-fit results of tephra loading and airborne ash dispersal. First, we summarize the results of the Fine Enriched TGSD. Then, we report the ESPs retrieved for the explored input TGSDs. The last sections refer to the validation of the reconstruction of the main eruption features by means of field, satellite, and AERONET observations, respectively.

### 5.1. ESP Estimation Solving the Inverse Problem

Regarding the tephra loading, Table 4 reports the results of the statistical analysis for the input parameter ranges (Table 2) with the different TGSDs. They indicate a minimum value of  $k = 2.96$  associated with the bi-Weibull distribution, whereas the Field, bi-Gaussian, and Fine Enriched TGSDs yield  $k = 3.36$ ,  $k = 3.37$ , and  $k = 3.37$ , respectively. Additionally, the  $RMSE_1$  and  $RMSE_2$  show similar values with a slight better performance for the bi-Weibull distribution. In other words, without considering other observations than the tephra loadings, the goodness-of-fit method presents the bi-Weibull distribution as best input TGSD for the simulations. The statistical values (Table 4) indicate an uncertainty on the TEM estimation of about a factor 2–3, similar to other classical methods (Bonadonna et al., 2015; Bonadonna & Costa, 2012, 2013).

The absence of PM<sub>10</sub> within the Field, bi-Gaussian, and bi-Weibull TGSDs (Figure 4) motivated to empirically modifying the Fine Enriched TGSD (section 4.4 and Figure 4). The comparative results for the PM<sub>10</sub> fractions (i.e., 0.3–1.3%) are reported in Table 5. They revealed a systematic AAM overestimation compared to the satellite retrievals (Table 6) for fractions higher than 0.5%. The statistical analysis (section 4.5 and Appendix B) indicates a best TGSD with 0.4% of PM<sub>10</sub> (i.e.,  $\gamma = 0.53$ ) to reproduce the AAM. Indeed, Table 5 shows for  $\gamma = 0.53$  a  $K$  index close to 1 and a minimum  $k$  around 1.3 (the  $RMSEs$  are also near the minimum). It follows that we selected the Fine Enriched TGSD modified with  $\gamma = 0.53$  (i.e., PM<sub>10</sub> = 0.4%). However, such a fraction does not permit the numerical reproduction of the maxima AAM per unit area, which is captured with a PM<sub>10</sub> fraction of 1.3% (i.e.,  $\gamma = 0.70$ ; Figure S2 in the supporting information).

Regardless of the TGSD used, the simulations return a column height of ~8.7 km a.s.l., which is consistent with the in situ observations (i.e., ~9 km a.s.l.) from INGV-OE (Figure 1c). The relationship between the column height and the MER gives very similar values of MER:  $1.2 \times 10^6$ ,  $1.4 \times 10^6$ ,  $1.3 \times 10^6$ , and  $1.3 \times 10^6$  kg/s for the Field, bi-Gaussian, bi-Weibull, and Fine Enriched TGSDs, respectively. The inverted exit velocity is obtained at 250 m/s, being similar to the value observed by Donnadieu et al. (2016). The  $\beta$  entrainment coefficient is calibrated by comparing both TEM released during the eruption (i.e.,  $K$  optimization) and mean MER estimated from the column height by using FPlume. The resulting  $\beta$  values range from 0.53 to 0.55, which are similar to the value estimated by Devenish et al. (2010).

### 5.2. Tephra Loading Validation Against Field Observations

Figure 5 compares the 10 tephra loadings measured at the sampled sites with the simulated values obtained for the Field, bi-Gaussian, bi-Weibull, and Fine Enriched TGSDs. The sensitivity to the input TGSD can be seen from both Table 1 and Figure 5. Regardless of the TGSD, the 10 simulated values lie within a factor of 10 the measurements. In particular, 8 of the 10 loadings are between 1/5- and 5-times the observed values. The computed values of the proximal samples (labels 1–7) range between ~11 and ~4.5 kg/m<sup>2</sup>, showing a narrower span than the field samples (~32 to ~1.2 kg/m<sup>2</sup>). Medial samples (labels 8 and 9 in Figure 5) are slightly overestimated. The farthest sample (label 10 in Figure 5) is either overestimated or underestimated tephra

**Table 5**  
Computed Airborne Ash Mass Time Series for Different  $\gamma$  Together With the Statistical Analysis

Time (UTC)	Fine Enriched TGSD with					
	$\gamma = 0.50$ (PM <sub>10</sub> = 0.3%)	$\gamma = 0.53$ (PM <sub>10</sub> = 0.4%)	$\gamma = 0.55$ (PM <sub>10</sub> = 0.5%)	$\gamma = 0.60$ (PM <sub>10</sub> = 0.7%)	$\gamma = 0.65$ (PM <sub>10</sub> = 0.9%)	$\gamma = 0.70$ (PM <sub>10</sub> = 1.3%)
	AAM (in kg, Computed AAM/Observed AAM)					
19:00	1.0 × 10 <sup>7</sup> (2.62)	1.3 × 10 <sup>7</sup> (3.43)	1.6 × 10 <sup>7</sup> (4.16)	2.3 × 10 <sup>7</sup> (5.84)	3.3 × 10 <sup>7</sup> (8.49)	4.7 × 10 <sup>7</sup> (12.16)
19:15	1.4 × 10 <sup>7</sup> (0.98)	1.8 × 10 <sup>7</sup> (1.30)	2.1 × 10 <sup>7</sup> (1.48)	3.1 × 10 <sup>7</sup> (2.24)	4.4 × 10 <sup>7</sup> (3.11)	6.3 × 10 <sup>7</sup> (4.47)
19:30	1.3 × 10 <sup>7</sup> (0.60)	1.7 × 10 <sup>7</sup> (0.79)	2.0 × 10 <sup>7</sup> (0.95)	2.8 × 10 <sup>7</sup> (1.34)	4.1 × 10 <sup>7</sup> (1.96)	5.6 × 10 <sup>7</sup> (2.69)
19:45	1.2 × 10 <sup>7</sup> (0.62)	1.6 × 10 <sup>7</sup> (0.84)	1.9 × 10 <sup>7</sup> (1.01)	2.8 × 10 <sup>7</sup> (1.46)	3.9 × 10 <sup>7</sup> (2.07)	5.4 × 10 <sup>7</sup> (2.84)
20:00	1.1 × 10 <sup>7</sup> (1.00)	1.5 × 10 <sup>7</sup> (1.39)	1.8 × 10 <sup>7</sup> (1.62)	2.7 × 10 <sup>7</sup> (2.49)	3.8 × 10 <sup>7</sup> (3.44)	5.4 × 10 <sup>7</sup> (4.93)
20:15	1.1 × 10 <sup>7</sup> (2.21)	1.5 × 10 <sup>7</sup> (3.08)	1.8 × 10 <sup>7</sup> (3.64)	2.6 × 10 <sup>7</sup> (5.31)	3.7 × 10 <sup>7</sup> (7.80)	5.1 × 10 <sup>7</sup> (10.65)
Statistical metric						
RMSE <sub>1</sub>	0.33	0.24	0.29	0.79	1.47	2.45
RMSE <sub>2</sub>	0.28	0.28	0.39	1.01	1.77	2.90
K	1.28	0.96	0.81	0.55	0.39	0.28
k	1.28	1.29	1.26	1.30	1.28	1.31
Bias	0.0	0.0	0.0	0.0	0.1	0.1
Correlation	0.3	0.1	0.5	-0.1	0.3	-0.1
t test	0.2	0.8	0.2	0.0	0.0	0.0

Note. Airborne ash masses (AAMs) are computed for different  $\gamma$  values used to produce the Fine Enriched total grain-size distribution (TGSD). Values inside parentheses refer to the ratio between computed and measured ash masses.

**Table 6**  
*Time Series of the Main Satellite Retrievals*

Time (UTC)	19:00	19:15	19:30	19:45	20:00	20:15
Cloud top temperature (°C)	-54.2	-53.5	-53.5	-53.8	-49.9	-48.6
Cloud top altitude (m a.s.l.)	9,321	9,167	9,167	9,167	8839	8,678
Airborne ash mass (kg)	$3.9 \times 10^6$	$1.4 \times 10^7$	$2.1 \times 10^7$	$1.9 \times 10^7$	$1.1 \times 10^7$	$4.8 \times 10^6$
Effective radius ( $\mu\text{m}$ )	4.33	4.13	4.24	4.21	4.58	4.71

Note. Retrievals derived from SEVIRI data and come from 15-min internal observation.

loading, depending on the input TGSD. Proximal samples show a slight enrichment in coarse material for the bi-Gaussian distribution than the other TGSDs (Figure 4), explaining the larger tephra loading estimates. In contrast, the lack of fine particle results on underestimating in load the farthest sample of about a factor 10.

Figure 6 displays the tephra loading maps obtained with the four input TGSDs. It shows that the bi-Gaussian and bi-Weibull distributions fail to reproduce the tephra loading up to distal areas, whereas the maps

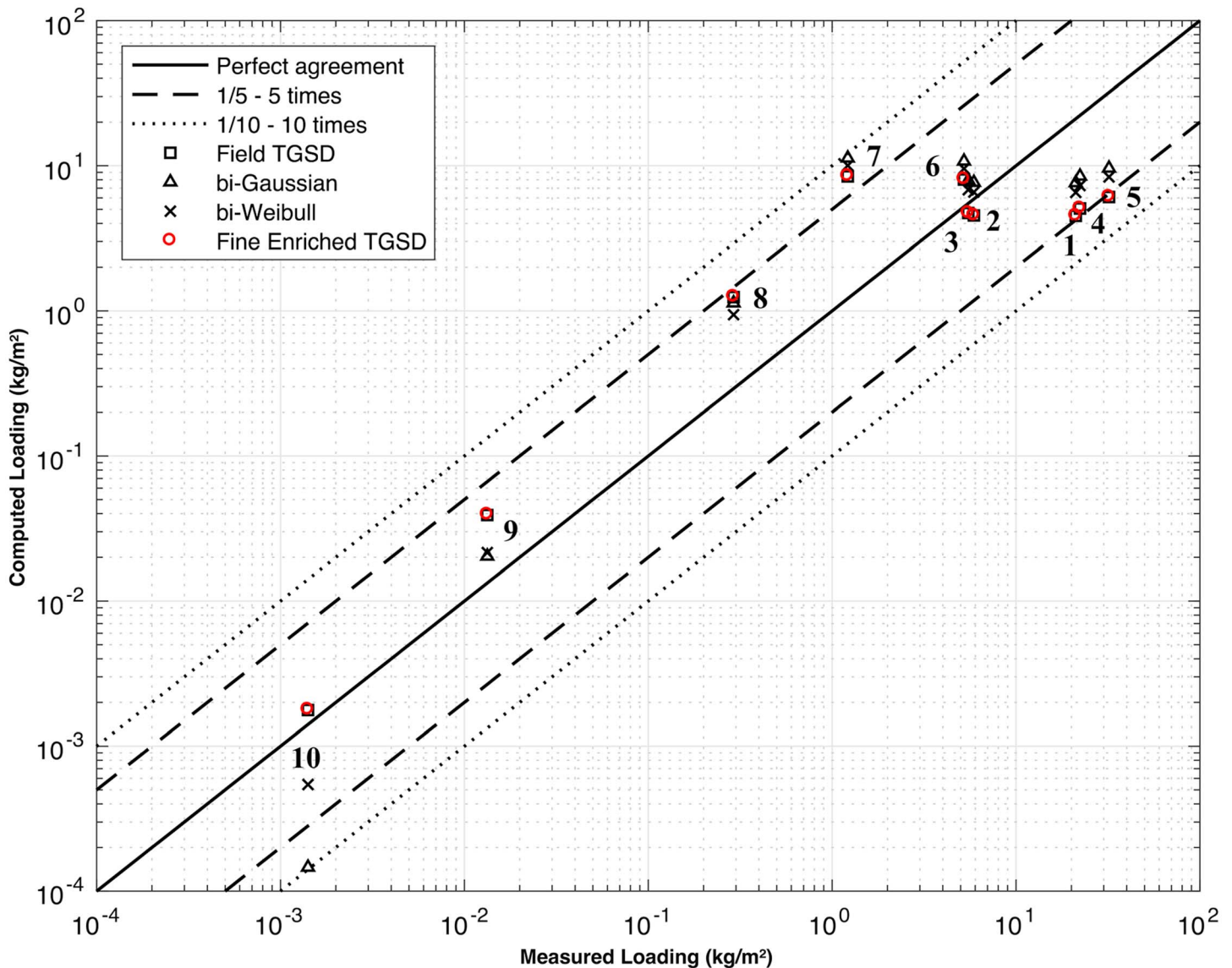


**Figure 5.** Observed tephra loadings versus computed data at 10 observation sites for the different input total grain-size distributions (TGSDs) used within the modeling simulations (details in Table 1). The typical errors are assumed of ~5–20% as described in Bonadonna et al. (2015).

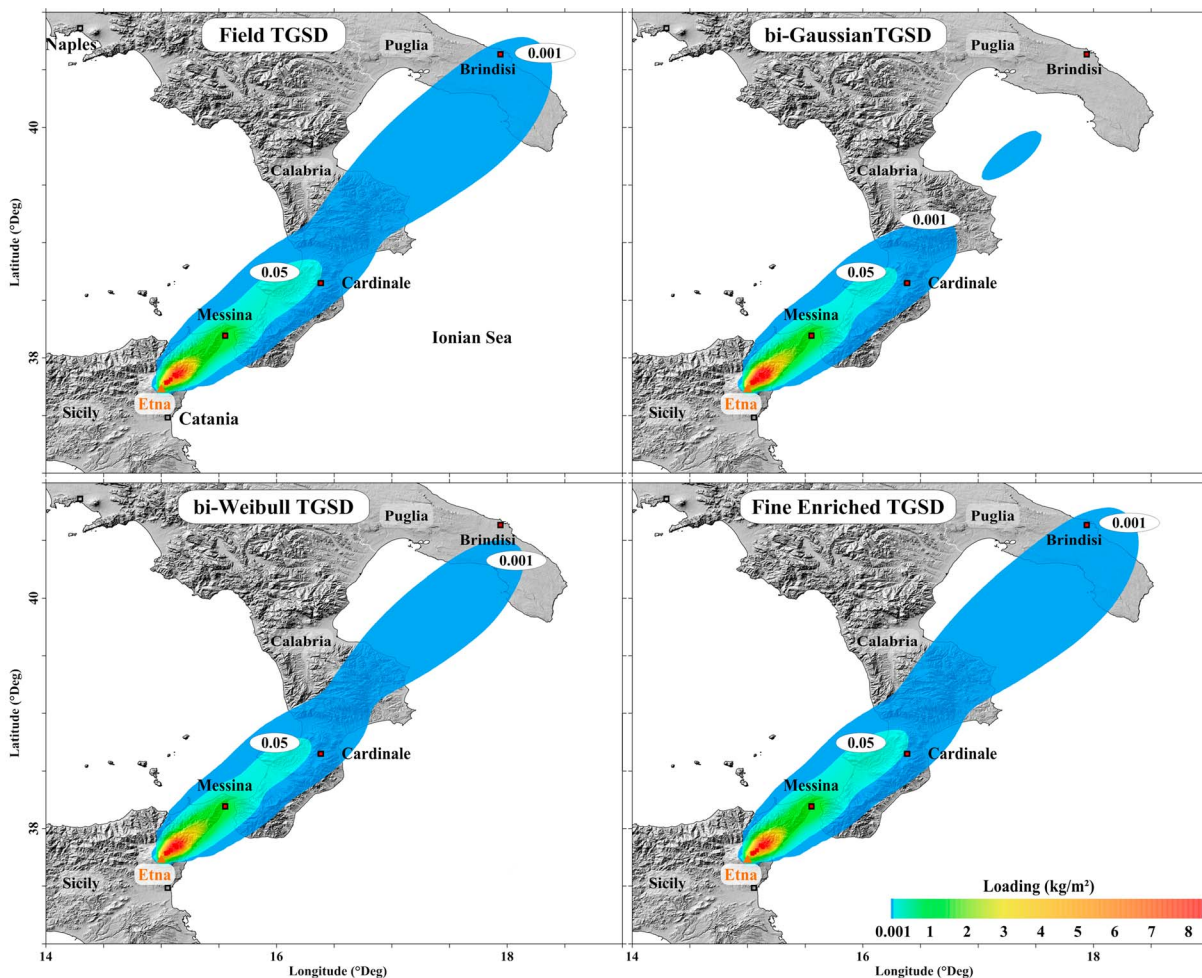


**Figure 6.** Tephra loading maps obtained for the different input total grain-size distributions (TGSDs; time series for the Fine Enriched TGSD is available as supporting information, Animation A1).

associated with the Field and Fine Enriched TGSDs capture reasonably well all sites (Table 1). The corresponding time evolution of the tephra loading for the Fine Enriched TGSD is available as supporting information (Animation A1).

Considering an eruption duration of 1 hr and 6 min through a constant eruptive phase (i.e., a unique column height), FPlume estimated the MER, which is used to assess the TEM. The optimal simulations selected for the different input TGSDs yield a TEM of  $4.8 \times 10^9$ ,  $5.3 \times 10^9$ ,  $4.8 \times 10^9$ , and  $4.9 \times 10^9$  kg for the Field, bi-Gaussian, bi-Weibull, and Fine Enriched TGSDs, respectively. The numerical TEM estimations are of the same order of magnitude than the field-derived TEM (i.e.,  $\sim 2.0 \pm 0.5 \times 10^9$  kg; section 4.1).

### 5.3. PM<sub>10</sub> Validation Against Satellite Observations

Among the explored input distributions, only the Fine Enriched TGSD has enough PM<sub>10</sub> (here 0.4% in weight) to inject enough particles to reproduce the far-traveling airborne ash mass retrieved from satellite data (Table 6). The airborne ash dispersion is shown in Figure 7, where the FALL3D results (a–d) are compared with the SEVIRI retrievals (e–h). The first-time window (in Figures 7a and 7e; 19:15 UTC) refers to 1 hr after the paroxysm started. It shows the PM<sub>10</sub> fraction injected into the atmosphere spreading toward the Calabrian region. The volcanic cloud elevation estimated from the SEVIRI data indicates that it already reached its maximum altitude at  $\sim 9.3$  km a.s.l. (Table 5). Hereinafter, we report the difference in terms of (1) total AAM and (2) maximum ash mass per unit area (all the values are reported in Table 4). At 19:15 UTC, the total AAM retrieved from SEVIRI returns  $1.4 \times 10^7$  kg, whereas FALL3D estimates  $1.8 \times 10^7$  kg (i.e.,  $\sim 30\%$  higher). The maximum ash mass per unit area measured from SEVIRI is  $\sim 22$  g/m<sup>2</sup>, while the computed value is  $\sim 12$  g/m<sup>2</sup>. The

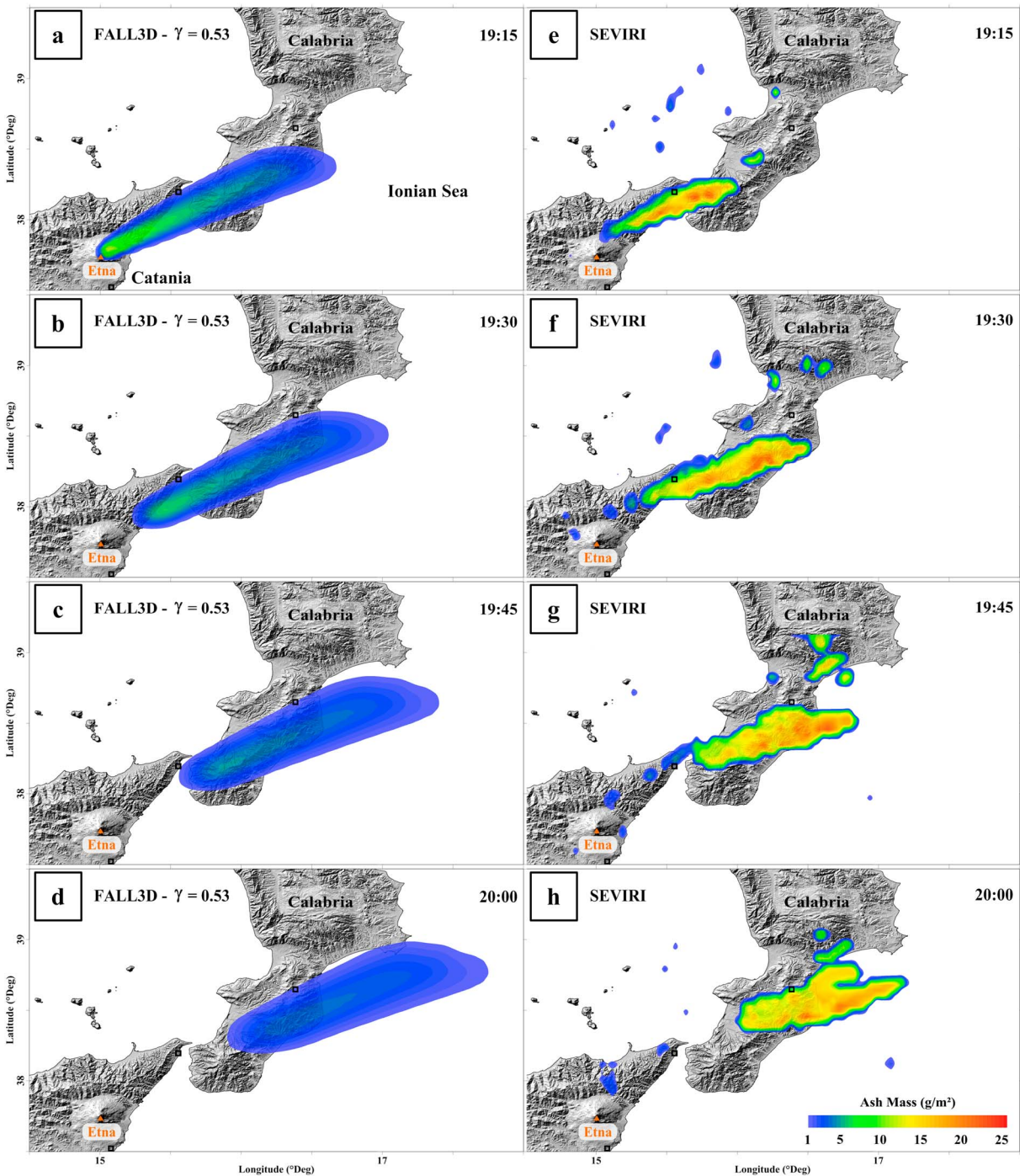


**Figure 7.** Airborne ash mass computed by FALL3D (a–d) and observed from satellite (e–h) from 19:15 to 20:00 UTC. Simulations correspond to the Fine Enriched total grain-size distribution obtained for  $\gamma = 0.53$ . The time-series animation is available as supporting information (Animation A2). SEVIRI = Spinning Enhanced Visible and Infrared Imager.

second-time window (19:30 UTC) illustrates the dispersal over the Calabria 15 min later. The total AAM estimated from SEVIRI is  $2.1 \times 10^7$  kg while the simulated value is  $1.7 \times 10^7$  kg (i.e., underestimation by  $\sim 21\%$ ). In this case, the maximum ash mass per unit area from SEVIRI ( $\sim 20$  g/m<sup>2</sup>) is about three times the simulated value ( $\sim 6$  g/m<sup>2</sup>). On the third-time window (19:45 UTC), satellite retrieval returns a total AAM of  $1.9 \times 10^7$  kg, whereas FALL3D gives  $1.6 \times 10^7$  kg (i.e., underestimation by  $\sim 16\%$ ). The simulation of the maximum ash mass per unit area is about four times lower than the retrieved one ( $\sim 5$  versus  $\sim 22$  g/m<sup>2</sup>,

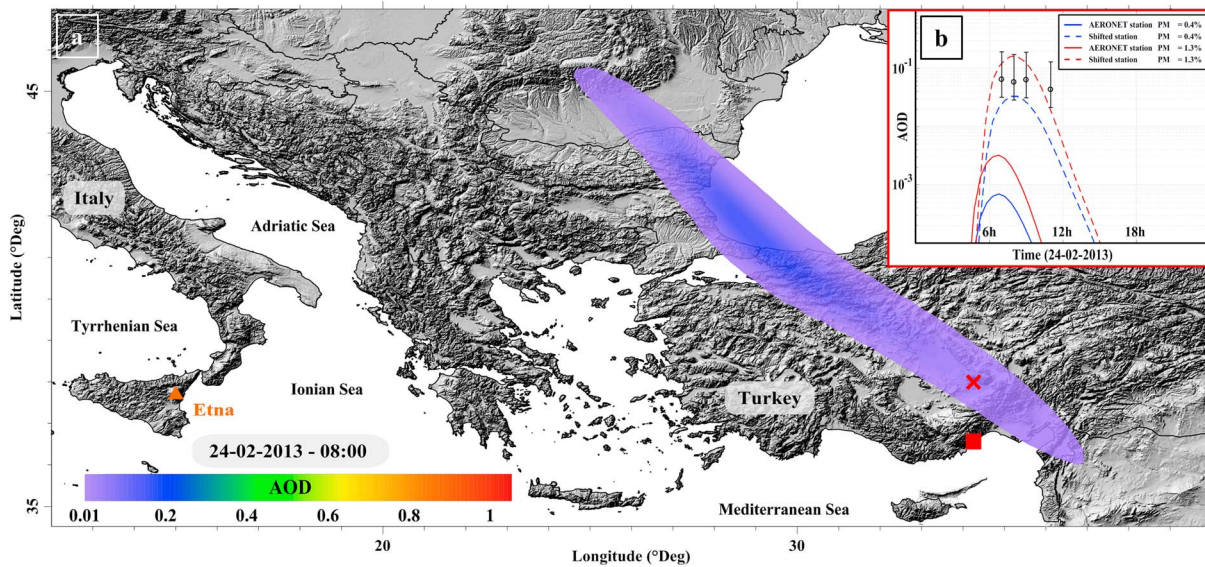


**Figure 8.** (a) Simulated aerosol optical depth (AOD) of the 23 February 2013 eruption for a computational domain extending over Turkey at 08:00 UTC (24 February 2013). The time series animation is available as supporting information (Animation A3). The red square refers to the Aerosol Robotic Network (AERONET) station (labeled IMS-METU ERDEMLI), whereas the red cross is the virtual point located two grid-nodes northward. (b) AOD comparison between the AERONET measurements (circles) and the numerical results over both the AERONET station and the shifted station for PM<sub>10</sub> fractions of 0.4% and 1.3%, respectively. The measurement uncertainty is estimated accordingly to Marengo et al. (2011).

respectively). The last time window (in Figures 7d and 7h; 20:00 UTC) shows the volcanic ash cloud over the Ionian Sea at a slightly lower altitude (Table 5). The total AAM are  $1.1 \times 10^7$  kg and  $1.5 \times 10^7$  kg (i.e., overestimation by  $\sim 39\%$ ) from SEVIRI and FALL3D, respectively. Again, the simulation of the maximum ash mass per unit area is about five times lower than the retrieved one ( $\sim 4$  versus  $\sim 21$  g/m<sup>2</sup>, respectively). The full time-series of the airborne ash simulation is available as supporting information (Animation A2).

These results show that the simulation obtained using the Fine Enriched TGSD (section 4.4) reproduces AAM correctly but do not capture the local maxima. In general, the computed ash mass within the volcanic cloud (in Figures 7a–7d) appears to be much more diluted than the satellite retrievals (Figures 7e–7h). From a computational point of view, to reproduce the correct local maxima, the input TGSD needs a PM<sub>10</sub> fraction about three times higher (i.e., 1.3 wt%). However, this implies an overestimation of the total AAM by a factor 6 in average (see Figure S2 in the supporting information).

#### 5.4. AOD Validation Against AERONET Observations

As an independent validation of the simulation results described above, we use the AOD measurements obtained from the AERONET (Holben et al., 1998). On 24 February 2013, an AERONET station (Figure 8a) detected particles over the Çamlıbel village (Turkey;  $\sim 1,700$  km from Etna) from 06:58 to 11:58 UTC. To compare the retrieved AODs with the computed values associated with the presence of volcanic ash at such distal areas, we considered the data relative to nonspherical particles only, as described in section 4.3. From 06:58–10:58 UTC, the average particle sphericity is retrieved by AERONET between 0.3 and 3.9, whereas at 11:58 UTC the value is 46.9 (hereinafter excluded). The corresponding AOD ranged between  $\sim 0.28$  and  $0.30$  (hereinafter AOD<sub>AERONET</sub>). As mentioned in section 4.3, we subtracted the Saharan dust contribution (i.e.,  $\sim 0.23$ ; GEOS-chem) from the AOD<sub>AERONET</sub> to assess the AOD associated with the volcanic ash over the Turkish station (hereinafter AOD<sub>ash</sub>). The resulting AOD<sub>ash</sub> ranges from  $\sim 0.05$  to  $0.07$  (Figure 8b).

We compared AOD<sub>ash</sub> with the numerical AOD (hereinafter AOD<sub>FALL3D</sub>) computed by FALL3D for the Fine Enriched TGSD. Figure 8a shows we extended the domain including the southern Europe with a 10-km grid resolution. The time series of AOD<sub>FALL3D</sub> shows a spreading over Albania, Greece, Macedonia, Serbia, Turkey, Bulgaria, Romania, Moldova, and Ukraine up to the Black Sea and the Russian borders (see Animation A3 in the supporting information). The comparative study (Figure 8b) indicates that AOD<sub>FALL3D</sub> reproduces two orders of magnitude smaller than AOD<sub>ash</sub> (i.e.,  $4.3 \times 10^{-4}$ ). Such a discrepancy is likely attributed mostly to the spatial-temporal shift of the meteorological fields due to the coarse resolution of the raw database (Dacre et al., 2011; Folch et al.,



2012) used for the simulation (e.g., Poret et al., 2017). In fact, comparing with  $AOD_{FALL3D}$  computed two grid-nodes northward ( $\sim 150$  km from the station),  $AOD_{FALL3D}$  improved substantially being similar to the  $AOD_{ash}$  with  $\sim 0.02$  (Figure 8a). It is worth noting that  $AOD_{FALL3D}$  is obtained with  $PM_{10} = 0.4\%$  for the Fine Enriched TGSD, which is selected on the basis of the total AAM analysis. However, considering  $PM_{10} = 1.3\%$  (section 5.3),  $AOD_{ash}$  became  $8.6 \times 10^{-4}$  and  $\sim 0.10$  over the Çamlıbel and the two grid-nodes shifted sites, respectively. Although this comparative study has a large uncertainty for both AOD estimations and spatiotemporal delay of meteorological model, we bear in mind that we used AOD observations for simulation results validation only, without constraining the model inputs. Besides these limitations, we note that Fine Enriched TGSD seems able to capture the concentration of ultrafine ash up to very distal areas ( $\sim 1,700$  km from source).

## 6. Discussion

This study proposes integrating field and satellite data of the 23 February 2013 Etna eruption to constrain the numerical reconstruction of the tephra loading and airborne ash mass. However, the input parameter interdependency implies the non-uniqueness solution through diverse ESP combinations (Anderson & Segall, 2013; Bonasia et al., 2010; Connor & Connor, 2005; Scollo et al., 2008). Although all the simulations capture reasonably the main features associated with the tephra loading, the Field, bi-Gaussian, and bi-Weibull TGSDs fail to best-fit simultaneously field and satellite data. In particular, only the Fine Enriched TGSD succeeds in reproducing both the tephra loading and airborne ash mass. This argues the need for developing an integrated method for assessing the initial grain-size distribution covering the entire size spectrum.

Considering GSD at the sampled sites, we compared each measurement with the numerical one (Figure 3) for the Fine Enriched TGSD. Overall, FALL3D captures 7 of the 10 GSDs by peaking at the same modes. However, two of the three most proximal samples (i.e., Casetta and Bivio 007 in Figure 3) are shifted by  $1 \Phi$ , which indicates coarser tephra deposits than the computed ones. In contrast, the Castiglione site (Figure 3) shows a finer field deposit than the computed one. These discrepancies can be attributed not only to the sample positions from the main plume axis but also to the sampling distance from the source (Spanu et al., 2016). In fact, the coarser material ( $-4 \geq \Phi \geq -2$ ) deposits within a narrow area from the vent, highlighting the difficulty to correctly capture the coarse tail distribution through the Voronoi tessellation method when the deposit is not adequately sampled (Andronico, Scollo, Cristaldi, et al., 2014).

Regarding the comparative study of the tephra loadings (Figure 5), the proximal measurements range from 32 to 1.2 kg/m<sup>2</sup>, whereas the computed are between 11 to 4.5 kg/m<sup>2</sup>. These results are assumed acceptable as they are within the same order of magnitude (e.g., Costa et al., 2014; Folch et al., 2010; Scollo et al., 2008). Although the tephra loadings are not perfectly reproduced, the resulting values indicate a consistency with the field measurements by lying within the 1/5–5 times limits for five of the seven proximal samples, whereas the two others are within the 1/10–10 times limits. The difference between the computed and measured proximal tephra loadings can be partially attributed, among others, to the low meteorological resolution. Indeed, for simulating several hundred kilometers domain, we used a  $4 \times 4$ -km meteorological resolution (Figure S1 in the supporting information), which means only five grid nodes are representing the proximal samples (located between  $\sim 5$  and  $\sim 16$  km from the source).

Satellite retrievals were integrated into field data by inverting the  $PM_{10}$  fraction to use within the input TGSD. However, focusing on reproducing the AAM per unit area suggests a  $PM_{10}$  content of 0.4%, whereas capturing the local maxima requires a larger fraction ( $\sim 1.3\%$ ). As most of Eulerian models, FALL3D has a numerical diffusion effect, which can partially explain the  $PM_{10}$  fraction discrepancy (Folch, 2012; Folch et al., 2012). Meanwhile, satellite retrievals have well-known ash discrimination issues associated with the BTM method. Indeed, spectral features in the thermal infrared may not allow a perfect discrimination of ash (see Guéhenneux et al., 2015, for a review). Additionally, atmospheric effects, such as convective clouds (Potts & Ebert, 1996) or mineral dust (Watkin, 2003), may produce negative BTM leading to false ash pixels detection. In contrast, moisture rich environment confounds BTM retrievals by adding a positive component (Pavolonis et al., 2006). These biases can affect the determination of the area containing airborne ash overestimating its extension.

Other complications can be attributed to the effect of ash aggregation, although for explosive basaltic eruptions (e.g., those ones from Etna) should not be significant (Rose & Durant, 2009). Indeed, the best simulations accounting for ash aggregation under the scheme developed in Costa et al. (2010) returns a contribution of only  $\sim 2$  wt% over the fine ash. Such results are obtained for an effective aggregate diameter  $\Phi_{Agg}$  of 2 and a density of 1,000 kg/m<sup>3</sup>. As expected, ash aggregation appears negligible compared to the TEM.

The use of the Fine Enriched TGSD permitted capturing the observed tephra loading and airborne ash mass, providing a more realistic estimation of the initial magma fragmentation down to the very fine ash distribution compared to the field-derived TGSD. However, such a characterization still needs further work in terms of (1) parameterization of the partial GSD for satellite retrievals or (2) integration of field and remote-sensing tephra measurements, also for other eruptions benefiting from large data set. At this stage, we opted for a purely empirical approach, but a more theoretical study is the object of ongoing research (Poret et al., 2018). It is worth noting that the used inversion of the very fine ash distribution is done comparing with satellite retrievals, which assume a lognormal distribution. This comparison can introduce a bias in the results without considering for the satellite-derived GSD. However, this study aims at dealing specifically with the reconstruction of the ESP leading to simultaneously capturing the tephra loading and airborne ash dispersal using information relative to coarse and very fine tephra. Also, the results we reported aim at encouraging future work that integrates data from field, ground-based instruments (e.g., visible and infrared images, weather and Doppler radars, light detection and ranging systems, and AERONET network), and satellite sensors (e.g., SEVIRI) to converge toward a full reconstruction of the tephra dispersal and deposition.

The findings of this study have implications for volcanic hazards and the evaluation of the related impacts. In fact, assessing accurately the initial magma fragmentation contributes to a more realistic description of both tephra deposition and airborne ash dispersal. On one hand, the tephra can affect the populations in the vicinity of the volcano (e.g., fallout and tephra accumulation hazards; Andronico et al., 2015). On the other hand, fine ash has high impact both near the source with the effects of  $PM_{10}$  on public health (Andronico & Del Carlo, 2016; Horwell, 2007; Horwell et al., 2013, 2017; Tomašek et al., 2016) and far away from the volcano with threat on air traffic (Casadevall, 1994; Casadevall et al., 1999; Guffanti et al., 2005). Quantifying airborne ash (i.e.,  $PM_{10}$ ) released during the 23 February 2013 lava fountain,  $PM_{10}$  dispersed in the atmosphere remaining above  $2 \text{ g/m}^2$  for 6 hr after the paroxysm up to several hundreds of kilometers from the source (see section 5.3 and Figures 7 and S2). Such a situation may pose hazards to air traffic safety highlighting again the necessity for assessing accurately the TGSD. As example, on December 2015, the Voragine crater of Etna produced four intense lava fountains within 3 days (Corsaro et al., 2017; Pompilio et al., 2017; Vulpiani et al., 2016). These similar episodes had sustained columns (i.e., high MERs) up to 15 km a.s.l. producing significant fine ash dispersed to distal regions. Although fine ash fraction during basaltic explosive eruptions represents a small fraction of the TEM, neglecting it within the TGSD can lead to a substantial underestimation of the far-traveling airborne ash mass, with implications for aviation safety. We showed that a better  $PM_{10}$  characterization is possible by adopting an integrated approach, which use models and all the available observations. We also encourage developing similar integrated approaches to other volcanoes for real-time forecast of tephra dispersal.

## 7. Concluding Remarks

On 23 February 2013, Etna volcano, Sicily, produced an intense lava fountain under strong north-easterly wind direction. The erupted tephra was deposited downwind from the volcano to the Puglia region, located  $\sim 410$  km from the source. These untypical meteorological conditions gave a rare opportunity to collect field samples from proximal to distal locations. This study aims at numerically reconstructing tephra loading and airborne ash mass by means of field, satellite (SEVIRI), and ground-based (AERONET) retrievals. Among the input eruption source parameters required by FALL3D, a better estimation of the TGSD accounting for both field and satellite measurements was demonstrated and evaluated. In fact, the long residence time of very fine ash into the atmosphere prevents deposition at reasonable distances. To better characterize the very fines, we parameterized the field-based TGSD through a bi-lognormal and bi-Weibull distribution. None of the two latter TGSDs can provide a very fine ash fraction allowing the computation of any far-traveling airborne ash up to distal areas. For this reason, we suggested here the empirical modification of the field-based TGSD to include the very fine ash by assuming a power law decay of the tail of the distribution. The Fine Enriched TGSD is similar to other Etna eruptions with a more marked bimodal distribution peaking at  $-3 \Phi$  and  $0.5 \Phi$  for the coarse- and fine-grained subpopulations, respectively. Eruption source parameters are inverted by means of a goodness-of-fit method best-reproducing simultaneously the tephra loading measurements and airborne ash mass retrieved by satellite. Results indicate a column height of 8.7 km a.s.l., a TEM of  $\sim 4.9 \times 10^9$  kg, a MER of  $\sim 1.3 \times 10^6$  kg/s for a paroxysmal phase of 1 hr and 6 min, a  $PM_{10}$  fraction of  $\sim 0.4$ – $1.3$  wt% with respect to the TEM, and an aggregate fraction of  $\sim 2$  wt% of the fine ash. These encouraging results highlight the need for integrating further airborne/airspace multisensors with field measurements to better characterize the parameters

controlling plume transport in the atmosphere and tephra sedimentation, with emphasis on the very fine ash distribution (PM<sub>10</sub>) responsible for public health and air traffic safety issues.

## Appendix A

Appendix A completes Tables 2 and 4 by reporting the other parameters and models used to run the simulations.

Parameterization	Description
Eruption duration (min)	66
Vent elevation (m a.s.l.)	3200
Vent longitude (°)	15.002012
Vent latitude (°)	37.746548
Time step meteo data (min)	30
Longitude nodes	100
Latitude nodes	111
Altitude layers(from 0 m a.s.l., 500-m step)	10,000
Eruption column model	FPlume <sup>a</sup>
Terminal velocity model	Ganser <sup>b</sup>
Vertical turbulence model	Similarity <sup>c</sup>
Horizontal turbulence model	CMAQ <sup>d</sup>
Gravity current	Yes <sup>e</sup>

*Note.* The computational domain extension starts at 9.75 and 34.5 (longitude/latitude in degrees) and ends at 40.5 and 52.5 (longitude/latitude in degrees).

<sup>a</sup>The eruption column model uses the buoyant plume theory (Folch et al., 2016). <sup>b</sup>The terminal settling velocity is calculated with the Ganser (1993) model. <sup>c</sup>The vertical component of the eddy diffusivity tensor ( $K_z$ ) is estimated using the similarity option (Costa et al., 2006; Ulke, 2000). <sup>d</sup>The horizontal component of the eddy diffusivity tensor ( $K_h$ ) is evaluated as in Byun and Schere (2006) by the CMAQ option. <sup>e</sup>The gravity current effects in the umbrella region, although negligible, were considered in the simulations (Costa et al., 2013; Suzuki & Koyaguchi, 2009).

## Appendix B

The input parameters are inverted by means of the normalized root mean square error (*RMSE*) as defined by the following:

$$RMSE_j = \sqrt{\sum_i^N w_j (Sim_i - Obs_i)^2}$$

$$w_{j=1} = \frac{1}{\sum_i^N Obs_i^2}$$

$$w_{j=2} = \frac{1}{N \times Obs_i^2}$$

where  $w_j$  refers to the weighting factor used within the *RMSE* calculation,  $i$  corresponds to the  $i$ th sample over a set of  $N$ .  $Obs_i$  and  $Sim_i$  are the observed and simulated tephra loadings, respectively. The weights correspond to different assumptions on the error distribution (Aitken, 1935; Costa et al., 2009). The  $RMSE_1$  is calculated with  $w_1$  referring to a constant absolute error, whereas the  $RMSE_2$  considers a constant relative error by implying the proportional weighting factor  $w_2$  (Bonasia et al., 2012; Folch et al., 2010; Poret et al., 2017).

## Notation

AAM	Airborne Ash Mass (in kg)
AERONET	AErosol RObotic NETwork
AOD	Aerosol Optical Depth (dimensionless)
BTD	Brightness Temperature Difference

ECMWF	European Center for Medium-range Weather Forecasts
ESP	Eruption Source Parameters
INGV-OE	Istituto Nazionale di Geofisica e Vulcanologia—Osservatorio Etneo
GSD	Grain-Size Distribution
MER	Mass Eruption Rate (in kg/m <sup>2</sup> )
MOCAGE	MOdèle de Chimie Atmosphérique à Grande Echelle
NAME	Numerical Atmospheric-dispersion Modeling Environment
NASA	National Aeronautics and Space Administration
NSEC	New Southeast Crater
OPGC	Observatoire de Physique du Globe de Clermont-Ferrand
PHOTONS	PHotométrie pour le Traitement Opérationnel de Normalisation Satellitaire
PM <sub>10</sub>	Particle Matter Below 10 μm
RMSE	Root Mean Square Error
SEVIRI	Spinning Enhanced Visible and Infrared Imager
TEM	Total Erupted Mass (in kg)
TGSD	Total Grain-Size Distribution
TIR	Thermal InfraRed
VAAC	Volcanic Ash Advisory Center

#### Acknowledgments

Figures S1 and S2 and Animations A1, A2, and A3 serves for illustrating the results and are available in the supporting information. This work is supported by the FP 7 Marie Curie Actions Framework (FP7-PEOPLE-2013-ITN), volcanic ash: field, experimental, and numerical investigations of processes during its lifecycles (VERTIGO project; grant agreement number 607905). A.C., D.A., and S.S. acknowledge the European project EUROVOLC (grant agreement number 731070) and the MIUR project Premiale Ash-RESILIENCE. We are grateful to M.G. and S. Costa for the rare ash sample collected in Cardinale and to ARPA Puglia for the Brindisi sample. Meteorological data were provided by the European Center for Medium-range Weather Forecasts. Data about dust contribution were provided by the GEOS-Chem model from the National Aeronautics and Space Administration Goddard Modeling and Assimilation Office (GMAO). We are grateful to Marco Neri and Boris Behncke for the fruitful discussions and the photo of the lava fountain. We also warmly acknowledge Ka Lok Chan for his help regarding the AOD comparison. We are deeply grateful to A. Marti, L. Mastin, I.M. Watson, anonymous reviewers, and Associate Editors for the criticism and constructive revision aimed to improve the quality and clarity of the manuscript.

#### References

- Aida, I. (1978). Reliability of a tsunami source model derived from fault parameters. *Journal of Physics of the Earth*, 26(1), 57–73. <https://doi.org/10.4294/jpe1952.26.57>
- Aitken, A. C. (1935). On least squares and linear combinations of observations. *Proceedings of the Royal Society of Edinburgh*, 55, 42–48.
- Allard, P., Burton, M., & Murè, F. (2005). Spectroscopic evidence for a lava fountain driven by previously accumulated magmatic gas. *Nature*, 433(7024), 407–410. <https://doi.org/10.1038/nature03246>
- Anderson, K., & Segall, P. (2013). Bayesian inversion of data from effusive volcanic eruptions using physics-based models: Application to Mount St. Helens 2004–2008. *Journal of Geophysical Research: Solid Earth*, 118, 2017–2037. <https://doi.org/10.1002/jgrb.50169>
- Andronico, D., Cristaldi, A., & Scollo, S. (2008). The 4–5 September 2007 lava fountain at South-East Crater of Mt. Etna, Italy. *Journal of Volcanology and Geothermal Research*, 173(3–4), 325–328. <https://doi.org/10.1016/j.jvolgeores.2008.02.004>
- Andronico, D., & Del Carlo, P. (2016). PM<sub>10</sub> measurements in urban settlements after lava fountain episodes at Mt. Etna, Italy: Pilot test to assess volcanic ash hazard on human health. *Natural Hazards and Earth System Sciences*, 16(1), 29–40. <https://doi.org/10.5194/nhess-16-29-2016>
- Andronico, D., Scollo, S., & Cristaldi, A. (2015). Unexpected hazards from tephra fallouts at Mt. Etna: The 23 November 2013 lava fountain. *Journal of Volcanology and Geothermal Research*, 304, 118–125. <https://doi.org/10.1016/j.jvolgeores.2015.08.007>
- Andronico, D., Scollo, S., Cristaldi, A., & Caruso, S. (2008). The 2002–03 Etna explosive activity: Tephra dispersal and features of the deposit. *Journal of Geophysical Research*, 113, B04209. <https://doi.org/10.1029/2007JB005126>
- Andronico, D., Scollo, S., Cristaldi, A., & Lo Castro, M. D. (2014). Representivity of incompletely sampled fall deposits in estimating eruption source parameters: A test using the 12–13 January 2011 lava fountain deposit from Mt. Etna volcano, Italy. *Bulletin of Volcanology*, 76(10). <https://doi.org/10.1007/s00445-014-0861-3>
- Andronico, D., Scollo, S., Lo Castro, M. D., Cristaldi, A., Lodato, L., & Taddeucci, J. (2014). Eruption dynamics and tephra dispersal from the 24 November 2006 paroxysm at south-east crater, Mt. Etna, Italy. *Journal of Volcanology and Geothermal Research* 274, 78–91. <https://doi.org/10.1016/j.jvolgeores.2014.01.009>
- Azzopardi, F., Ellul, R., Prestifilippo, M., Scollo, S., & Coltelli, M. (2013). The effect on Etna volcanic ash clouds on the Maltese Islands. *Journal of Volcanology and Geothermal Research*, 260, 13–26. <https://doi.org/10.1016/j.jvolgeores.2013.04.019>
- Bagheri, G., & Bonadonna, C. (2016). On the drag of freely falling non-spherical particles. *Powder Technology*, 301, 526–544. <https://doi.org/10.1016/j.powtec.2016.06.015>
- Barsotti, S., Andronico, D., Neri, A., Del Carlo, P., Baxter, P. J., Aspinall, W. P., & Hincks, T. (2010). Quantitative assessment of volcanic ash hazards for health and infrastructure at Mt. Etna (Italy) by numerical simulation. *Journal of Volcanology and Geothermal Research*, 192(1–2), 85–96. <https://doi.org/10.1016/j.jvolgeores.2010.02.011>
- Barsotti, S., Neri, A., & Scire, J. (2008). The VOL-CALPUFF model for atmospheric ash dispersal. I. Approach and physical formulation. *Journal of Geophysical Research*, 113, B03208. <https://doi.org/10.1029/2006JB004623>
- Beckett, F. M., Witham, C. S., Hort, M. C., Stevenson, J. A., Bonadonna, C., & Millington, S. C. (2014). The sensitivity of NAME forecasts of the transport of volcanic ash clouds to the physical characteristics assigned to the particles. Met Office, *Forecasting Research*, Technical report n°592.
- Beckett, F. M., Witham, C. S., Hort, M. C., Stevenson, J. A., Bonadonna, C., & Millington, S. C. (2015). Sensitivity of dispersion model forecasts of volcanic ash clouds to the physical characteristics of the particles. *Journal of Geophysical Research: Atmospheres*, 120, 11,636–11,652. <https://doi.org/10.1002/2015JD023609>
- Behncke, B., Branca, S., Corsaro, R. A., De Beni, E., Miraglia, L., & Proietti, P. (2014). The 2011–2012 summit activity of Mount Etna: Birth, growth and products of the new SE crater. *Journal of Volcanology and Geothermal Research*, 270, 10–21. <https://doi.org/10.1016/j.jvolgeores.2013.11.012>
- Bey, I., Jacob, D. J., Yantosca, R. M., Logan, J. A., Field, B. D., Fiore, A. M., et al. (2001). Global modeling of tropospheric chemistry with assimilated meteorology: Model description and evaluation. *Journal of Geophysical Research*, 106(D19), 23,073–23,095. <https://doi.org/10.1029/2001JD000807>

- Bonadonna, C., Biass, S., & Costa, A. (2015). Physical characterization of explosive volcanic eruptions based on tephra deposits: Propagation of uncertainties and sensitivity analysis. *Journal of Volcanology and Geothermal Research*, 296, 80–100. <https://doi.org/10.1016/j.jvolgeores.2015.03.009>
- Bonadonna, C., & Costa, A. (2012). Estimating the volume of tephra deposits: A new simple strategy. *Geology*, 40(5), 415–418. <https://doi.org/10.1130/G32769.1>
- Bonadonna, C., & Costa, A. (2013). Plume height, volume, and classification of explosive volcanic eruptions based on the Weibull function. *Bulletin of Volcanology*, 75(8), 742. <https://doi.org/10.1007/s00445-013-0742-1>
- Bonadonna, C., Genco, R., Gouhier, M., Pistolesi, M., Cioni, R., Alfano, F., et al. (2011). Tephra sedimentation during the 2010 Eyjafjallajökull eruption (Iceland) from deposit, radar, and satellite observations. *Journal of Geophysical Research*, 116, B12202. <https://doi.org/10.1029/2011JB008462>
- Bonadonna, C., & Houghton, B. F. (2005). Total grain-size distribution and volume of tephra-fall deposits. *Bulletin of Volcanology*, 67(5), 441–456. <https://doi.org/10.1007/s00445-004-0386-2>
- Bonasia, R., Costa, A., Folch, A., Macedonio, G., & Capra, L. (2012). Numerical simulation of tephra transport and deposition of the 1982 El Chichón eruption and implications for hazard assessment. *Journal of Volcanology and Geothermal Research*, 231–232, 39–49. <https://doi.org/10.1016/j.jvolgeores.2012.04.006>
- Bonasia, R., Macedonio, G., Costa, A., Mele, D., & Sulpizio, R. (2010). Numerical inversion and analysis of tephra fallout deposits from the 472 AD sub-Plinian eruption at Vesuvius (Italy) through a new best-fit procedure. *Journal of Volcanology and Geothermal Research*, 189(3–4), 238–246. <https://doi.org/10.1016/j.jvolgeores.2009.11.009>
- Bursik, M. (2001). Effect of wind on the rise height of volcanic plumes. *Geophysical Research Letters*, 28(18), 3621–3624. <https://doi.org/10.1029/2001GL013393>
- Byun, D., & Schere, K. L. (2006). Review of the governing equations, computational algorithms, and other components of the Models-3 Community Multiscale Air Quality (CMAQ) modeling system. *Applied Mechanics Reviews*, 59(2), 51–77. <https://doi.org/10.1115/1.2128636>
- Carbone, D., Zuccarello, L., Messina, A., Scollo, S., & Rymer, H. (2015). Balancing bulk gas accumulation and gas output before and during lava fountaining episodes at Mt. Etna. *Scientific Reports*, 5(1), 18049. <https://doi.org/10.1038/srep18049>
- Casadevall, T. J. (1994). Volcanic ash and aviation safety. Proceedings of the First International Symposium on Volcanic Ash and Aviation Safety. USGS Bull. 2047, p. 450.
- Casadevall, T. J., Thompson, T. B., & Fox, T. (1999). World map of volcanoes and principal aeronautical features. *USGS Map I-2700*, scale 1:34,268,000, reprinted 2001.
- Chan, K. L., & Chan, K. L. (2017). Aerosol optical depths and their contributing sources in Taiwan. *Journal of Atmospheric Environment*, 148, 364–375. <https://doi.org/10.1016/j.atmosenv.2016.11.011>
- Cigala, V., Kueppers, U., Peña Fernández, J. J., Taddeucci, J., Sesterhenn, J., & Dingwell, D. B. (2017). The dynamics of volcanic jets: Temporal evolution of particles exit velocity from shock-tube experiments. *Journal of Geophysical Research: Solid Earth*, 122, 6031–6045. <https://doi.org/10.1002/2017JB014149>
- Connor, C., Hill, B., Winfrey, B., Franklin, M., & La Femina, P. (2001). Estimation of volcanic hazards from tephra fallout. *Natural Hazards Review*, 2(1), 33–42. [https://doi.org/10.1061/\(ASCE\)1527-6988\(2001\)2:1\(33\)](https://doi.org/10.1061/(ASCE)1527-6988(2001)2:1(33))
- Connor, L. J., & Connor, C. B. (2005). Inversion is the key to dispersion: Understanding eruption dynamics by inverting tephra fallout. In *Statistics in volcanology* (pp. 231–242). London: Geological Society.
- Corradini, S., Montopoli, M., Guerrieri, L., Ricci, M., Scollo, S., Merucci, L., et al. (2016). A multi-sensor approach for the volcanic ash cloud retrievals and eruption characterization. *Remote Sensing, Special Issue on Volcano Remote Sensing*, 8(1), 58. <https://doi.org/10.3390/rs8010058>
- Corradini, S., Spinetti, C., Carboni, E., Tirelli, C., Buongiorno, M. F., Pugnaghi, S., & Gangale, G. (2008). Mt. Etna tropospheric ash retrieval and sensitivity analysis using Moderate Resolution Imaging Spectroradiometer measurements. *Journal of Applied Remote Sensing*, 2(1), 023550. <https://doi.org/10.1117/1.3046674>
- Corsaro, R. A., Andronico, D., Behncke, B., Branca, S., De Beni, E., Caltabiano, T., et al. (2017). Monitoring the December 2015 summit eruptions of Mt. Etna (Italy): Implications on eruptive dynamics. *Journal of Volcanology and Geothermal Research*, 341, 53–69. <https://doi.org/10.1016/j.jvolgeores.2017.04.018>
- Corsaro, R. A., & Miraglia, L. (2013a). Composizione dei vetri dei prodotti emessi dal Nuovo Cratere di Sud-Est durante le fontane di lava del 23 e 28 febbraio 2013, INGV Report. Retrieved from <http://www.ct.ingv.it/it/rapporti/vulcanologia.html?view=docman>
- Corsaro, R. A., & Miraglia, L. (2013b). Composizione dei vetri dei prodotti emessi dal Nuovo Cratere di Sud-Est durante la fontana di lava del 23 novembre 2013, INGV Report. Retrieved from <http://www.ct.ingv.it/it/rapporti/vulcanologia.html?view=docman>
- Costa, A., Dell'Erba, F., Di Vito, M. A., Isaia, R., Macedonio, G., Orsi, G., & Pfeiffer, T. (2009). Tephra fallout hazard assessment at the Campi Flegrei caldera (Italy). *Bulletin of Volcanology*, 71(3), 259–273. <https://doi.org/10.1007/s00445-008-0220-3>
- Costa, A., Folch, A., & Macedonio, G. (2010). A model for wet aggregation of ash particles in volcanic plumes and clouds: 1. Theoretical formulation. *Journal of Geophysical Research*, 115, B09201. <https://doi.org/10.1029/2009JB007175>
- Costa, A., Folch, A., & Macedonio, G. (2013). Density-driven transport in the umbrella region of volcanic clouds: Implications for tephra dispersion models. *Geophysical Research Letters*, 40, 4823–4827. <https://doi.org/10.1002/grl.50942>
- Costa, A., Folch, A., Macedonio, G., Giaccio, B., Isaia, R., & Smith, V. C. (2012). Quantifying volcanic ash dispersal and impact from Campanian Ignimbrite super-eruption. *Geophysical Research Letters*, 39, L10310. <https://doi.org/10.1029/2012GL051605>
- Costa, A., Macedonio, G., & Folch, A. (2006). A three-dimensional Eulerian model for transport and deposition of volcanic ashes. *Earth and Planetary Science Letters*, 241(3–4), 634–647. <https://doi.org/10.1016/j.epsl.2005.11.019>
- Costa, A., Pioli, L., & Bonadonna, C. (2016). Assessing tephra total grain-size distribution: Insights from field data analysis. *Earth and Planetary Science Letters*, 443, 90–107. <https://doi.org/10.1016/j.epsl.2016.02.040>
- Costa, A., Pioli, L., & Bonadonna, C. (2017). Corrigendum to "Assessing tephra total grain-size distribution: Insights from field data analysis". (*Earth and Planetary Science Letters* 443, 90–107, 2016). *Earth and Planetary Science Letters*. <https://doi.org/10.1016/j.epsl.2017.03.003>
- Costa, A., Smith, V. C., Macedonio, G., & Matthews, N. E. (2014). The magnitude and impact of the Youngest Toba Tuff super-eruption. *Frontiers in Earth Science*, 2, 16. <https://doi.org/10.3389/feart.2014.00016>
- Costa, A., Suzuki, Y. J., Cerminara, M., Devenish, B., Esposti Ongaro, T., Herzog, M., et al. (2016). Results of the eruption column model inter-comparison study. *Journal of Volcanology and Geothermal Research*, 326. <https://doi.org/10.1016/j.jvolgeores.2016.01.017>
- Dacre, H. F., Grant, A. L. M., Hogan, R. J., Belcher, S. E., Thomson, D. J., Devenish, B. J., et al. (2011). Evaluating the structure and magnitude of the ash plume during the initial phase of the 2010 Eyjafjallajökull eruption using lidar observations and NAME simulations. *Journal of Geophysical Research*, 116, D00U03. <https://doi.org/10.1029/2011JD015608>

- De Beni, E., Behncke, B., Branca, S., Nicolosi, I., Carluccio, R., D'Ajello Caracciolo, F., & Chiappini, M. (2015). The continuing story of Etna's New Southeast Crater (2012-2014): Evolution and volume calculations based on field surveys and aerophotogrammetry. *Journal of Volcanology and Geothermal Research*, 303, 175–186. <https://doi.org/10.1016/j.jvolgeores.2015.07.021>
- Dellino, P., & Kyriakopoulos, K. (2003). Phreatomagmatic ash from the ongoing eruption of Etna reaching the Greek island of Cefalonia. *Journal of Volcanology and Geothermal Research*, 126(3–4), 341–345. [https://doi.org/10.1016/S0377-0273\(03\)00154-9](https://doi.org/10.1016/S0377-0273(03)00154-9)
- Devenish, B. J., Rooney, G. G., Webster, H. N., & Thomson, D. J. (2010). The entrainment rate for buoyant plumes in a cross-flow. *Boundary-Layer Meteorology*, 134(3), 411–439. <https://doi.org/10.1007/s10546-009-9464-5>
- Donnadiu, F., Freville, P., Hervier, C., Coltelli, M., Scollo, S., Prestifilippo, M., et al. (2016). Near-source Doppler radar monitoring of tephra plumes at Etna. *Journal of Volcanology and Geothermal Research*, 312, 26–39. <https://doi.org/10.1016/j.jvolgeores.2016.01.009>
- Dubovik, O. (2004). Optimization of numerical inversion in photopolarimetric remote sensing. In G. Videen, Y. Yatskiv, & M. Mishchenko (Eds.), *Photopolarimetry in remote sensing* (pp. 65–106). Dordrecht, Netherlands: Kluwer Academic.
- Dubovik, O., & King, M. D. (2000). A flexible inversion algorithm for retrieval of aerosol optical properties from Sun and sky radiance measurements. *Journal of Geophysical Research*, 105(20), 673–696.
- Dubovik, O., Sinyuk, A., Lapyonok, T., Holben, B. N., Mishchenko, M., Yang, P., et al. (2006). Application of spheroid models to account for aerosol particle nonsphericity in remote sensing of desert dust. *Journal of Geophysical Research*, 111, D11208. <https://doi.org/10.1029/2005JD006619>
- Dubovik, O., Smirnov, A., Holben, B. N., King, M. D., Kaufman, Y. J., Eck, T. F., & Slutsker, I. (2000). Accuracy assessment of aerosol optical properties retrieval from AERONET sun and sky radiance measurements. *Journal of Geophysical Research*, 105(D8), 9791–9806. <https://doi.org/10.1029/2000JD900040>
- Fairlie, T. D., Jacob, D. J., & Park, R. J. (2007). The impact of transpacific transport of mineral dust in the United States. *Journal of Atmospheric Environment*, 41(6), 1251–1266. <https://doi.org/10.1016/j.atmosenv.2006.09.048>
- Folch, A. (2012). A review of tephra transport and dispersal models: Evolution, current status, and future perspectives. *Journal of Volcanology and Geothermal Research*, 235–236, 96–115. <https://doi.org/10.1016/j.jvolgeores.2012.05.020>
- Folch, A., Costa, A., & Basart, S. (2012). Validation of the FALL3D ash dispersion model using observations of the 2010 Eyjafjallajökull volcanic ash clouds. *Atmospheric Environment*, 48, 165–183. <https://doi.org/10.1016/j.atmosenv.2011.06.072>
- Folch, A., Costa, A., Durant, A., & Macedonio, G. (2010). A model for wet aggregation of ash particles in volcanic plumes and clouds: 2. Model application. *Journal of Geophysical Research*, 115, B09202. <https://doi.org/10.1029/2009JB007176>
- Folch, A., Costa, A., & Macedonio, G. (2009). FALL3D: A computational model for transport and deposition of volcanic ash. *Computers and Geosciences*, 35(6), 1334–1342. <https://doi.org/10.1016/j.cageo.2008.08.008>
- Folch, A., Costa, A., & Macedonio, G. (2016). FPLUME-1.0: An integral volcanic plume model accounting for ash aggregation. *Geoscientific Model Development*, 9(1), 431–450. <https://doi.org/10.5194/gmd-9-431-2016>
- Ganser, G. H. (1993). A rational approach to drag prediction of spherical and non-spherical particles. *Powder Technology*, 77(2), 143–152. [https://doi.org/10.1016/0032-5910\(93\)80051-B](https://doi.org/10.1016/0032-5910(93)80051-B)
- Gouhier, M., Guéhenneux, Y., Labazuy, P., Cacault, P., Decriem, J., & Rivet, S. (2016). HOTVOLC: A web-based monitoring system for volcanic hot spots. *Geological Society, London, Special Publications*, 426, SP426–SP431.
- Grindle, T. J., & Burcham, F. W. (2003). Engine damage to a NASA DC-8-72 airplane from a high-altitude encounter with a diffuse volcanic ash cloud. National Aeronautics and Space Administration, Dryden Flight Research Center, Edwards, California, Report NASA/TM-2003-212030
- Guéhenneux, Y., Gouhier, M., & Labazuy, P. (2015). Improved space borne detection of volcanic ash for real-time monitoring using 3-band method. *Journal of Volcanology and Geothermal Research*, 293, 25–45. <https://doi.org/10.1016/j.jvolgeores.2015.01.005>
- Guffanti, M., Ewert, J. W., Gallina, G. M., Bluth, G. J. S., & Swanson, G. L. (2005). Volcanic-ash hazard to aviation during the 2003–2004 eruption activity of Anatahan volcano Commonwealth of the Northern Mariana Islands. *Journal of Volcanology and Geothermal Research*, 146(1–3), 241–255. <https://doi.org/10.1016/j.jvolgeores.2004.12.011>
- Holben, B. N., Eck, T. F., Slutsker, I., Smirnov, A., Sinyuk, A., Schafer, J., et al. (2006). Aeronet's version 2.0 quality assurance criteria. *Proceedings of SPIE 6408, Remote Sensing of the Atmosphere and Clouds*, 64080Q. <https://doi.org/10.1117/12.706524>
- Holben, B. N., Eck, T. F., Slutsker, I., Tanré, D., Buis, J. P., Setzer, A., et al. (1998). AERONET—A federated instrument network and data archive for aerosol characterization. *Remote Sensing of Environment*, 66(1), 1–16. [https://doi.org/10.1016/S0034-4257\(98\)00031-5](https://doi.org/10.1016/S0034-4257(98)00031-5)
- Horwell, C. J. (2007). Grain size analysis of volcanic ash for the rapid assessment of respiratory health hazard. *Journal of Environmental Monitoring*, 9(10), 1107–1115. <https://doi.org/10.1039/b710583p>
- Horwell, C. J., Baxter, P. J., Hillman, S. E., Calkins, J. A., Damby, D. E., Delmelle, P., et al. (2013). Physicochemical and toxicological profiling of ash from the 2010 and 2011 eruptions of Eyjafjallajökull and Grimsvötn volcanoes, Iceland using a rapid respiratory hazard assessment protocol. *Environmental Research*, 127, 63–73. <https://doi.org/10.1016/j.envres.2013.08.011>
- Horwell, C. J., Sargent, P., Andronico, D., Lo Castro, M. D., Tomatis, M., Hillman, S. E., et al. (2017). The iron-catalysed surface reactivity and health-pertinent physical characteristics of explosive volcanic ash from Mt. Etna, Italy. *Journal of Applied Volcanology*, 6(1). <https://doi.org/10.1186/s13617-017-0063-8>
- Kaminski, E., Tait, S., & Carazzo, G. (2005). Turbulent entrainment in jets with arbitrary buoyancy. *Journal of Fluid Mechanics*, 526, 361–376. <https://doi.org/10.1017/S0022112004003209>
- Krumbein, W. C. (1934). Size frequency distributions of sediments. *Journal of Sedimentary Research*, 4, 65–67.
- Lo Castro, M. D., & Andronico, D. (2008). Operazioni di base per la misura della distribuzione granulometrica di particelle vulcaniche tramite il CAMSIZER. *Rapporti Tecnici INGV*, 79, 1–35.
- Macedonio, G., Costa, A., & Longo, A. (2005). A computer model for volcanic ash fallout and assessment of subsequent hazard. *Computational Geosciences*, 31(7), 837–845. <https://doi.org/10.1016/j.cageo.2005.01.013>
- Macedonio, G., Costa, A., Scollo, S., & Neri, A. (2016). Effects of eruption source parameter variation and meteorological dataset on tephra fallout hazard assessment: Example from Vesuvius (Italy). *Journal of Applied Volcanology*, 5(1), 5. <https://doi.org/10.1186/s13617-016-0045-2>
- Marenco, F., Johnson, B., Turnbull, K., Newman, S., Haywood, J., Webster, H., & Ricketts, H. (2011). Airborne lidar observations of the 2010 Eyjafjallajökull volcanic ash plume. *Journal of Geophysical Research*, 116, D00U05. <https://doi.org/10.1029/2011JD016396>
- Martí, A., Folch, A., Costa, A., & Engwell, S. (2016). Reconstructing the Plinian and co-ignimbrite sources of large volcanic eruptions: A novel approach for the Campanian Ignimbrite. *Nature Communication – Science Report*, 6(1), 21220. <https://doi.org/10.1038/srep21220>
- Maryon, R. H., Ryall, D. B., & Malcolm, A. L. (1999). The NAME 4 dispersion model: Science documentation, turbulence and diffusion note no 262, Met Office.

- Mastin, L. G., Guffanti, M., Servranckx, R., Webley, P., Barsotti, S., Dean, K., et al. (2009). A multidisciplinary effort to assign realistic source parameters to models of volcanic ash-cloud transport and dispersion during eruptions. *Journal of Volcanology and Geothermal Research*, 186(1-2), 10–21. <https://doi.org/10.1016/j.jvolgeores.2009.01.008>
- Metrich, N., Allard, P., Spilliaert, N., Andronico, D., & Burton, M. (2004). 2001 flank eruption of the alkali- and volatile-rich primitive basalt responsible for Mount Etna's evolution in the last three decades. *Earth and Planetary Science Letters*, 228(1-2), 1–17. <https://doi.org/10.1016/j.epsl.2004.09.036>
- Metrich, N., & Rutherford, M. J. (1998). Low pressure crystallization paths of H<sub>2</sub>O-saturated basaltic-hawaiitic melts from Mt. Etna: Implications for open-system degassing volcanoes. *Geochimica et Cosmochimica Acta*, 62(7), 1195–1205. [https://doi.org/10.1016/S0016-7037\(98\)00048-9](https://doi.org/10.1016/S0016-7037(98)00048-9)
- Morton, B. R., Taylor, G. I., & Turner, J. S. (1956). Turbulent gravitational convection from maintained and instantaneous source. *Philosophical Transactions of the Royal Society of London: London, A*, 234(1196), 1–23. <https://doi.org/10.1098/rspa.1956.0011>
- Mueller, S. B., Ayris, P. M., Wadsworth, F. B., Kueppers, U., Casas, A. S., Delmelle, P., et al. (2017). Ash aggregation enhanced by deposition and redistribution of salt on the surface of volcanic ash in eruption plumes. *Nature Communication - Science Report*, 7, 45762. <https://doi.org/10.1038/srep45762>
- Mueller, S. B., Kueppers, U., Ametsbichler, J., Cimarelli, C., Merrison, J. P., Poret, M., et al. (2017). Stability of volcanic ash aggregates and break-up processes. *Nature Communication - Science Report*, 7, 7440. <https://doi.org/10.1038/s41598-017-07927-w>
- O'Neill, N. T., Eck, T. F., Smirnov, A., Holben, B. N., & Thulasiraman, S. (2003). Spectral discrimination of coarse and fine mode optical depth. *Journal of Geophysical Research*, 108(D17), 4559. <https://doi.org/10.1029/2002JD002975>
- Park, R. J., Jacob, D. J., Field, B. D., Yantosca, R. M., & Chin, M. (2004). Natural and transboundary pollution influences on sulfate-nitrate-ammonium aerosols in the United States: Implications for policy. *Journal of Geophysical Research*, 109, D15204. <https://doi.org/10.1029/2003JD004473>
- Pavlonis, M. J., Feltz, W. F., Heidinger, A. K., & Gallina, G. M. (2006). A daytime complement to the reverse absorption technique for improved automated detection of volcanic ash. *Journal of Atmospheric and Oceanic Technology*, 23(11), 1422–1444. <https://doi.org/10.1175/JTECH1926.1>
- Pompilio, M., Bertagnini, A., Del Carlo, P., & Di Roberto, A. (2017). Magma dynamics within a basaltic conduit revealed by textural and compositional features of erupted ash: The December 2015 Mt. Etna paroxysms. *Scientific Reports*, 7(1), 4805. <https://doi.org/10.1038/s41598-017-05065-x>
- Poret, M., Corradini, S., Merucci, L., Costa, A., Andronico, D., Montopoli, M., et al. (2018). Reconstructing volcanic plume evolution integrating satellite and ground-based data: application to the 23 November 2013 Etna eruption. *Atmospheric Chemistry and Physics*, 18, 4695–4714. <https://doi.org/10.5194/acp-18-4695-2018>
- Poret, M., Costa, A., Folch, A., & Marti, A. (2017). Modeling tephra dispersal and ash aggregation: The 26th April 1979 eruption, La Soufrière St. Vincent. *Journal of Volcanology and Geothermal Research*, 347, 207–220. <https://doi.org/10.1016/j.jvolgeores.2017.09.012>
- Potts, R. J., & Ebert, E. E. (1996). On the detection of volcanic ash in NOAA AVHRR infrared satellite imagery. Paper Presented at 8th Australian Remote Sens. Conf. Canberra, 25–29.
- Prata, A. J. (1989a). Observations of volcanic ash clouds in the 10–12 μm window using AVHRR/2 data. *International Journal of Remote Sensing*, 10, 4–5. 751–761.
- Prata, A. J. (1989b). Radiative transfer calculations for volcanic ash clouds. *Geophysical Research Letters*, 16(11), 1293–1296. <https://doi.org/10.1029/GL016i011p01293>
- Prata, A. J., & Grant, I. F. (2001). Retrieval of microphysical and morphological properties of volcanic ash plumes from satellite data: Application to Mt Ruapehu, New Zealand. *Quarterly Journal of the Royal Meteorological Society*, 127(576), 2153–2179. <https://doi.org/10.1002/qj.49712757615>
- Prata, A. J., & Kerkmann, J. (2007). Simultaneous retrieval of volcanic ash and SO<sub>2</sub> using MSGSEVIRI measurements. *Geophysical Research Letters*, 34, L05813. <https://doi.org/10.1029/2006GL022869>
- Rodgers, C. D. (2000). *Inverse methods for atmospheric sounding: Theory and practice*. Singapore: World Scientific Pub Co Inc.
- Rose, W. I., & Durant, A. J. (2009). Fine ash content of explosive eruptions. *Journal of Volcanology and Geothermal Research*, 186(1-2), 32–39. <https://doi.org/10.1016/j.jvolgeores.2009.01.010>
- Scollo, S., Boselli, A., Coltelli, M., Leto, G., Pisani, G., Spinelli, N., & Wang, X. (2012). Monitoring Etna volcanic plumes using a scanning LiDAR. *Bulletin of Volcanology*, 74(10), 2383–2395. <https://doi.org/10.1007/s00445-012-0669-y>
- Scollo, S., Coltelli, M., Bonadonna, C., & Del Carlo, P. (2013). Tephra hazard assessment at Mt. Etna (Italy). *Natural Hazards and Earth System Sciences Discussions*, 1(3), 2945–2981. <https://doi.org/10.5194/nhessd-1-2945-2013>
- Scollo, S., Folch, A., & Costa, A. (2008). A parametric and comparative study of different tephra fallout models. *Journal of Volcanology and Geothermal Research*, 176(2), 199–211. <https://doi.org/10.1016/j.jvolgeores.2008.04.002>
- Scollo, S., Prestifilippo, M., Pecora, E., Corradini, S., Merucci, L., Spata, G., & Coltelli, M. (2014). Eruption column height estimation of the 2011–2013 Etna lava fountains. *Annals of Geophysics*, 57(2), S0214. <https://doi.org/10.4401/ag-6396>
- Sič, B., El Amraoui, L., Marécal, V., Josse, B., Arteta, J., Guth, J., et al. (2015). Modeling of primary aerosols in the chemical transport model MOCAGE: Development and evaluation of aerosol physical parameterizations. *Geoscientific Model Development*, 8(2), 381–408. <https://doi.org/10.5194/gmd-8-381-2015>
- Smoluchowski, M. (1917). Veruch einer mathematischen Theorie der Koagulationkinetic kolloider Lösungen. *Zeitschrift für Physikalische Chemie*, 92, 128–168.
- Spanu, A., de Vitturi, M. M., & Barsotti, S. (2016). Reconstructing eruptive source parameters from tephra deposit: A numerical study of medium-sized explosive eruptions at Etna volcano. *Bulletin of Volcanology*, 78(9), 59. <https://doi.org/10.1007/s00445-016-1051-2>
- Spilliaert, N., Allard, P., Metrich, N., & Sobolev, A. V. (2006). Melt inclusion record of the conditions of ascent, degassing, and extrusion of volatile-rich alkali basalt during the powerful 2002 flank eruption of Mount Etna (Italy). *Journal of Geophysical Research*, 111, B04203. <https://doi.org/10.1029/2005JB003934>
- Stevenson, J. A., Millington, S. C., Beckett, F. M., Swindles, G. T., & Thordarson, T. (2015). Big grains go far: Understanding the discrepancy between tephrochronology and satellite infrared measurements of volcanic ash. *Atmospheric Measurement Techniques*, 8(5), 2069–2091. <https://doi.org/10.5194/amt-8-2069-2015>
- Sulpizio, R., Folch, A., Costa, A., Scaini, C., & Dellino, P. (2012). Hazard assessment of far-range volcanic ash dispersal from a violent Strombolian eruption at Somma-Vesuvius volcano, Naples, Italy: Implications on civil aviation. *Bulletin of Volcanology*, 74(9), 2205–2218. <https://doi.org/10.1007/s00445-012-0656-3>
- Suzuki, Y. J., & Koyaguchi, T. (2009). A three-dimensional numerical simulation of spreading umbrella clouds. *Journal of Geophysical Research*, 114, B03209. <https://doi.org/10.1029/2007JB005369>

- Suzuki, Y. J., & Koyaguchi, T. (2015). Effects of wind on entrainment efficiency in volcanic plumes. *Journal of Geophysical Research: Solid Earth*, *120*, 6122–6140. <https://doi.org/10.1002/2015JB012208>
- Tomašek, I., Horwell, C. J., Damby, D. E., Barošová, H., Geers, C., Petri-Fink, A., et al. (2016). Combined exposure of diesel exhaust particles and respirable Soufrière Hills volcanic ash causes a (pro-)inflammatory response in an in vitro multicellular epithelial tissue barrier model. *Particle and Fibre Toxicology*, *13*(1), 67. <https://doi.org/10.1186/s12989-016-0178-9>
- Twomey, S. (1996). *Introduction to the mathematics of inversion in remote sensing and indirect measurements*. New York: Dover Publications.
- Ulke, A. G. (2000). New turbulent parameterization for a dispersion model in atmospheric boundary layer. *Atmospheric Environment*, *34*(7), 1029–1042. [https://doi.org/10.1016/S1352-2310\(99\)00378-7](https://doi.org/10.1016/S1352-2310(99)00378-7)
- Vulpiani, G., Ripepe, M., & Valade, S. (2016). Mass discharge rate retrieval combining weather radar and thermal camera observations. *Journal of Geophysical Research: Solid Earth*, *121*, 5679–5695. <https://doi.org/10.1002/2016JB013191>
- Watkin, S. C. (2003). The application of AVHRR data for the detection of volcanic ash in a volcanic ash advisory centre. *Meteorological Applications*, *10*(4), 301–311. <https://doi.org/10.1017/S1350482703001063>
- Watson, I. M., & Oppenheimer, C. (2001). Photometric observations of Mt. Etna's different aerosol plumes. *Atmospheric Environment*, *35*(21), 3561–3572. [https://doi.org/10.1016/S1352-2310\(01\)00075-9](https://doi.org/10.1016/S1352-2310(01)00075-9)
- Watson, I. M., Realmuto, V. J., Rose, W. I., Prata, A. J., Bluth, G. J. S., Gu, Y., et al. (2004). Thermal infrared remote sensing of volcanic emissions using the moderate resolution imaging spectroradiometer. *Journal of Volcanology and Geothermal Research*, *135*(1-2), 75–89. <https://doi.org/10.1016/j.jvolgeores.2003.12.017>
- Watt, S. F. L., Gilbert, J. S., Folch, A., & Phillips, J. C. (2015). An example of enhanced tephra deposition driven by topographic induced atmospheric turbulence. *Bulletin of Volcanology*, *77*(5), 35. <https://doi.org/10.1007/s00445-015-0927-x>
- Wen, S., & Rose, W. I. (1994). Retrieval of sizes and total masses of particles in volcanic clouds using AVHRR bands 4 and 5. *Journal of Geophysical Research*, *99*(D3), 5421–5431. <https://doi.org/10.1029/93JD03340>
- Wilkins, K. L., Watson, I. M., Kristiansen, N. I., Webster, H. N., Thomson, D. J., Dacre, H. F., & Prata, A. J. (2016). Using data insertion with the NAME model to simulate the 8 May 2010 Eyjafjallajökull volcanic ash cloud. *Journal of Geophysical Research: Atmospheres*, *121*, 306–323. <https://doi.org/10.1002/2015JD023895>
- Witham, C. S., Hort, M. C., Potts, R., Servranckx, R., Husson, P., & Bonnardot, F. (2007). Comparison of VAAC atmospheric dispersion models using the 1 November 2004 Grimsvötn eruption. *Meteorological Applications*, *14*(1), 27–38. <https://doi.org/10.1002/met.3>